Experimental Demonstration and Exploration of Quantum Lattice Gas Algorithms

by

Zhiying Chen

Submitted to the Department of Nuclear Engineering
in partial fulfillment of the requirements for the degree of

Doctor of Philosophy in Nuclear Science and Engineering

at the

MASSACHUSETTS INSTITUTE OF TECHNOLOGY

February 2005

Author .....
Department of Nuclear Engineering
February, 2005

Certified by .....
David G. Cory
Professor
Thesis Supervisor

Read by .....
Terry Orlando
Professor
Thesis Reader

Accepted by .....
Jeffrey A. Coderre
Chairman, Department Committee on Graduate Students

Experimental Demonstration and Exploration of Quantum Lattice Gas Algorithms

by

Zhiying Chen

Submitted to the Department of Nuclear Engineering
on February, 2005, in partial fulfillment of the
requirements for the degree of
Doctor of Philosophy in Nuclear Science and Engineering

Abstract

Recently, it has been suggested that an array of small quantum information processors sharing classical information can be used to solve selected computational problems, referred to as a type-II quantum computer. The first concrete implementation demonstrated here solves the diffusion equation, and it provides a test example from which to probe the strengths and limitations of this new computation paradigm. The NMR experiment consists of encoding a mass density onto an array of 16 two-qubit quantum information processors and then following the computation through 7 time steps of the algorithm. The results show a good agreement with the analytic solution for diffusive dynamics.

From the numerical simulations of the NMR implementations, we explore two major error sources (1) the systematic error in the collision operator and (2) the linear approximation in the initialization. Since the mass density evolving under the Burgers equation develops sharp features over time, this is a stronger test of liquid state NMR implementations of type-II quantum computers than the previous example using the diffusion equation. Small systematic errors in the collision operator accumulate and swamp all other errors. We propose, and demonstrate, that the accumulation of this error can be avoided to a large extent by replacing the single collision operator with a set of operators, that have random errors and similar fidelities. Experiments have been implemented on 16 two-qubit sites for eight successive time steps for the Burgers equation. The improvement in the experimental results suggests that more complicated modulation of error terms may offer further improvement.

An alternative approach has been suggested to encode in the Fourier space (k-space) to remove the usage of this linear approximation. This new method also provides us a simple means to implement the streaming operation quantum mechanically by controlling magnetic field gradients sandwiched with RF pulses. Therefore, this method might serve as a new tool to probe the implementations of quantum lattice gas (QLG) algorithms. Experimental demonstration of the diffusion equation has been performed on 16 two-qubit sites for four successive time steps.

Recently, much attention has been focused on constructing many identical simple

processing elements arranged in a cellular automata architecture recently. It is likely that the early quantum hardware will be built in a similar manner. Quantum lattice gas algorithms therefore provide a bridge between such hardware and potential early algorithms. We propose a quantum lattice gas model similar to the one proposed by Margolus for the classical setting. This quantum algorithm simulates the one-particle quantum random walk. The preliminary experimental design associated with the lattice gas model on a ring molecule is presented. The searches for the suitable pulses to construct the unitary operators, used in the implementations of the lattice gas model, are done and the results are encouraging.

Thesis Supervisor: David G. Cory
Title: Professor

Acknowledgments

The first person that I would like to thank is my supervisor, David Cory, for his motivation, sound advice, guidance, firm encouragement and help. David's creative and fresh ideas have kept me busy. The fruitful experience working with him not only teaches my enormous scientific knowledge, but also the way to delivery the ideas and teamwork.

It is also my pleasure to thank Jeffrey Yepez, a wonderful and talented collaborator. In addition to his scientific knowledge, his willingness to explain our work and discuss new ways to approach the problems has made my life more enjoyable. I am also proud to have worked with Carlos Perez. The work presented in these pages contains many of his insights and contributions.

I am also grateful to the talented and enthusiastic people that have made this lab a dynamic place. I enjoyed the long streak working with Marco Pravia, thinking, and discussing. I especially want to thank to Paola Cappellaro for her consideration and willingness to spend time to discuss and explore my ideas. Yun Liu deserves special thanks for his enormous knowledge on computers as well as his insights into many fields. I am also thankful to Nicolas Boulant (Garcon), Hyong-Joon Cho, and Chandrasekhar Ramanathan for helping in many ways with experimental and simulation work. Many thanks go to my colleagues and the entire, evolving lab over the years.

The experience at MIT represents a significant portion of my life. The friendships I made in those days were extremely important. I deeply appreciate that my friends spent their precious time to assistant and guide me throughout the years.

I am most appreciate the constant love and support that my parents, Baoqiu and Zhongyu, and my sister Zhiqun have given me. Without their help, I would not have made it this far.

For my mother, farther, sister, and friends at MIT

Contents

1 Introduction **21**

2 Type-II Quantum Lattice Gas Algorithm **25**

2.1 Lattice Gas Method 25

2.2 The 1-D Diffusion Automaton 27

2.2.1 Microscopic Regime 27

2.2.2 Mesoscopic Regime 27

2.2.3 Macroscopic Regime 29

2.2.4 Transition Matrix 31

2.3 Type-II Quantum Lattice Gas Algorithm 32

3 NMR Demonstration **37**

3.1 Methodology for NMR Implementations 38

3.1.1 Spin System and Control 38

3.1.2 Lattice Initialization 41

3.1.3 Collision and Swap Gates 47

3.1.4 Measurement 49

3.1.5 Streaming 51

3.2 Experiment Demonstration 51

3.3 Conclusion 51

4 Systematic Error **55**

4.1 The Burgers Equation 56

4.1.1 QLG Algorithm for the Burgers Equation 56
4.1.2 First Implementation using NMR 58
4.1.3 The Collision Matrix with Higher Viscosity Term 61
4.1.4 Numerical Simulations 63
4.1.5 The Collision Operator with Modulated Phases 66
4.2 Conclusion 68
4.3 Other Error Sources 70
4.4 Discussion 70

5 Linear Approximation **73**
5.1 Mapping to k-space 74
5.2 NMR Implementation 75
5.2.1 Encoding 76
5.2.2 Collision 80
5.2.3 Measurement 82
5.2.4 Streaming 82
5.3 Conclusion and Discussion 84

6 Type-I Quantum Lattice Gas Algorithms **87**
6.1 Quantum lattice gas algorithms 88
6.2 Chain Architectures 92
6.3 NMR Simulations 94
6.3.1 Spin System 94
6.3.2 Logic Gates 95
6.3.3 Methodology 97

A Quantum Simulation using NMR **101**

List of Figures

3-1 **Labeled chloroform** Labeled chloroform consists of two qubits, the hydrogen nucleus and labeled carbon served as qubits 1 and 2. States $|0\rangle$ and $|1\rangle$ are the ground state and excited state, respectively, induced by the Zeeman interaction with the applied magnetic field. Frequencies w_1 and w_2, defined as multiplication of the gyro-magnetic ratio γ and the magnetic field B_0, are the resonant frequencies to flip the spins. . 38

3-2 **Liquid sample in the coils** The lattice initialization is demonstrated. The liquid sample is placed in the middle with the gradient coils on both ends and surrounded by the RF coils. Once the gradient field is turned on, the resonant frequencies across the sample will vary corresponding to the strength and duration of the gradient. Thus, the spin ensemble can be sliced into a lattice of small blocks. 40

3-3 **Quantum lattice gas algorithm for solving the 1-D diffusion equation.** The algorithm employs N two-qubit sites to encode the discretized mass density. Each site codes for a single value of the mass density using the quantum state of the two qubits. The encoded information is subjected to a series of local transformations that evolve the system. The collision operator C is the only entangling operation in the algorithm, and it creates quantum coherences limited to each two-qubit system. The streaming is executed by classical communication, and it moves the occupation numbers up and down the lattice as denoted by the arrows. The sectioned cylinder depicts the position of the sites in the NMR sample. Each site is physically realized as an addressable slice of isotropically-labeled chloroform solution. 42

3-4 **Equalizing magnetization** Since the ratio of γ_H to γ_C is a factor of four, the spectra of H and C following a $\frac{\pi}{2}$ pulse should reflect $4:1$ ratio in the peak heights, shown in (a). In order to compensate the different magnetization, the equalization pulse sequence is applied and results in the spectrum (b). 44

3-5 **Pseudo-pure states** The results of pseudo-pure states of hydrogen and carbon are shown in (a) and (b), respectively. 45

3-6 **NMR methodology for QLG algorithm.** The NMR implementation consists of four main sections, each corresponding to the prescribed QLG algorithm step. The top two lines in the diagram correspond to RF pulses applied to the proton and carbon qubits, respectively. The third line shows the application of magnetic field gradients. In the encoding section, the initial carbon magnetization is recorded on the protons before being transferred to the carbons. The starting magnetization is specified by using a RF pulse shaped as the Fourier transform of the desired magnetization. The shaped pulses are applied in the presence of gradients so that each site can be addressed. A carbon decoupling sequence prevents the scalar coupling from interfering with the low power shaped pulses. The $\frac{\pi}{2}$ at the end of the encoding move the information form the x-axis to the z-axis, as required by the QLG algorithm. The collision operator follows the encoding, and it is implemented without gradients to ensure that all of the sites in the sample feel the same transformation. The results are observed in two experiments, each time using the more sensitive proton channel. A swap gate is added when measuring the carbon magnetization. Finally, the streaming operation is applied by shifting the frequencies of the carbon and proton shapes in opposite directions. 48

3-7 **Pulse sequence for the collision operator** The collision operator for the diffusion equation can be generated by applying $\frac{\pi}{2}$ pulses on both channels with delay time $\frac{1}{4J}$ in between. The same sequence can be used to generate the swap gate by increasing the delay time to $\frac{1}{2J}$. 50

3-8 **QLG algorithm experimental results.** The experimental mass densities are plotted in the figure, together with plots of the analytical solution and the numerical simulation of the NMR experiment. Seven steps of the algorithm were implemented on 16 two-qubit sites. The simulations were performed using the actual RF nutation rates and times of the experimental setup. The calculations closely match the data, suggesting that the deviation between the analytical results and the data can be attributed imperfections in the methodology. As a result, the simulations promise to be useful in exploring the errors from alternate methods. 52

4-1 **QLG algorithm for the Burgers equation implemented in four steps.** Three horizontal lines represent proton spin, carbon spin and field gradients. Both starting magnetizations are encoded in proton channel first due to the high signal to noise ratio while decoupled in carbon channel to prevent interfering of scalar coupling. The collision operator is applied after the initialization. Measurement are also taken in two steps in the proton channel followed by data processing in a personal computer. 61

4-2 **Experiment results comparing with simulation and analytical solutions.** The experimental data (dots) are plotted together with the simulations (grey dash lines) and the analytical solutions (black solid lines) for 15 time steps on a lattice of 16 cells. The horizontal axis for each plot indicates the number of the lattice cells and vertical axis is the flow velocity. The numbers associated with each plot are the time steps. The deviation between the simulation and analytical solutions is mainly due to the accumulative errors in the collision operator. We also observed the deviation between the experimental data and simulation results, possibly introduced by inhomogeneity, self-diffusion. 62

4-3 **Experimental data** The experimental data (dots) are plotted, together with plots of the analytical solutions (solid lines) and the numerical simulations (dash lines) of the NMR experiment. Nine time steps (numbers) of the algorithm have been carried out on 16 two-qubit sites. The vertical axis is associated with flow speed and the horizontal axis presents the lattice sites. The simulations closely match the data, suggesting that the deviation between the analytical results and the data can be attributed to four imperfection controls, discussed below, in the implementations. 64

4-4 **Relative strength of four types of errors** We present the relative strength of each source here. Horizontal axis is denoted by time steps and vertical axis shows the difference between the simulation results with the analytical solutions. We notice that the deviation is mainly caused by the linear approximation at the beginning and the accumulated errors in the collision operators take over after a few time steps. 65

4-5 **Systematic errors** The growth of the systematic errors due to the collision operator in two NMR implementation. The single collision operator data (dots) is fit (solid line) with a line of slope 1, which shows linear growth of the error. The collision operator data with modulated phases (pluses) is the fit with a line of slope 3/4 (dashed line). The buildup of the systematic errors has been slowed down by proposed method. However, the systematic errors have not been totally converted into random errors. 67

4-6 **Experiment data versus analytical results** The experimental data are plotted together with the analytical solutions for 8 time steps on a lattice of 16 parallel two-qubit QIPs. Viscosity: $\frac{1}{4}\frac{\Delta x^2}{\Delta t}$. Experimental NMR data (dots) versus analytical solution (curves). Randomizing the error terms in the collision operator has improved the experimental results dramatically. 69

5-1 **One step in the initialization** One period of the sequence used in the initialization and corresponding changes of k values in the k-space are presented. The solid line, in the k space diagram, illustrates the shift of the wave number for the hydrogen spin while the time iterates forwards. The dash line gives the movement of k value for the carbon. At the end of the sequence, the wave numbers of the characteristic Fourier components of both spins are incremented by the same amount. Below the plot, the pulse sequence is demonstrated. 81

5-2 **Readout** Measurement on the hydrogen spin is illustrated here. The magnetization peaks are related to the occupation numbers at each lattice site by $n_i = \frac{1}{2}(1 + \sigma_z^i)$. The observed spectrum is imposed by a sinc function. 83

5-3 **k-space experimental data versus analytical solutions** The experimental data (dots) are plotted together with analytical solutions (solid lines) for four time steps on 16 two-qubit sites. 85

6-1 **Collision rules for 1D QLG algorithm** The collisions of the simplest one dimensional QLG algorithm. A single particle of mass $\tan\theta$ at a site has an amplitude to be scattered $i\sin\theta$. 89

6-2 **Partitioned cellular automata** Each square represents a cell, and each oval is a unitary operator acting on two lattice cells. On odd/even steps the pairing is exchanged. 91

6-3 **Spin chain architectures** One-dimensional array of quantum units ($ABCABC\ldots$), such as nuclear spins in a polymer, is decipted here. A series of spins ABC can be treated as a quantum information processor. Sequence of resonant pulses allow one to load information and unload results at the end of an array. Each processor has the same circuit and they can process information and exchange it with the nearest neighbors. 93

6-4 **The ring model** This model shows a chain of 6 quibts. Two loading qubits are presented by X and Y respectively. All the qubits with the same labels share the same resonant frequencies. 94

6-5 **The two-qubit SWAP gate** Here demonstrates the pulse sequence of the SWAP gate on two qubits and untouched the third spin. To refocus the scalar interactions between pair AC and BC, a π pulse has been performed on pair AB and separate the delay period to half. Two π pulses are performed on qubit C in the a quarter and three quarter of the delay respectively. 97

6-6 **One step QLG algorithm** The NMR implementation consists of three main section, each corresponding to the prescribed QCA step. The horizontal lines in the diagram correspond to RF pluses applied to each qubit respectively. In the encoding section, the initial magnetization is recorded on loading qubits before transferred to the other qubits. The unitary operator on pair AB and swap gate between BC follow the encoding. In the next step, the unitary operator on pair CA are applied, followed by swap gate between BC again. 99

A-1 **Quantum simulation scheme** Correspondence between the simulated and physical system. The initial state s evolves to $s(T)$ under the propagator U. This process is related to the evolution of state p in the physical system by an invertible map ϕ. 102

A-2 **Truncated quantum harmonic oscillator** NMR signals demonstrate a quantum simulation of truncated harmonic oscillator. The solid lines are fits to theoretical expectations. Evolution of the different initial states are shown: (a) evolution of $|0\rangle$ with no oscillation (b) evolution of $|0\rangle + i|2\rangle$, showing 2Ω oscillations (c) evolution of $|0\rangle + |1\rangle + |2\rangle + |3\rangle$, showing Ω oscillation and (d) 3Ω oscillations. . . 103

A-3 **Demonstration of system and environment** Basic model for the system, local quantum and classical environment. 104

A-4 **Decay rate** Simulation showing the dependence of the decay rate on the kick rate, and the onset of the decoupling limit. Beyond 900 *kicks/ms* the decay rate decreases. 105

List of Tables

6.1 **Summary of the relevant characteristics for the set of transformations required for the implementation of QCA.** The three columns list the pulse duration (in μs), maximum power (in kHz), and the fidelity of simulated pulse. 96

6.2 **Summary of the gates fidelities.** The two columns list the unitary operators, and the gate fidelity of them 98

Chapter 1

Introduction

In 1965 Intel co-founder Gordan Moore noted that the processing power (number of transistors and speed) of computer chips was almost doubling every 18 months. This trend has continued roughly since the first computer in 1946. Such an exponential and rapid acceleration in computing ability is impressive. However, the basic technologies that have enabled Moore's Law are reaching fundamental physical limits. The miniaturization of processor components, which has taken transistor sizes from one centimeter in 1965 to 0.1 microns today. If Moore's law continues unabated, then each transistor is predicted to be as small as a hydrogen atom by about 2030. At that size, the quantum nature of electrons in the atoms becomes significant. Current technologies cannot possibly continue miniaturization beyond the scale of atoms, and errors will be generated in the computation. However, it is possible to exploit the quantum physics as a new way to do computation. This new way opens up fantastic new computational power based on the superpositions of quantum states.

The field of quantum information processing (QIP) has made steady progress in the past decade, driven in part by the realization that some quantum algorithms offer a computational advantage over the best-known classical counterparts [1]. Integer factorization of large numbers is believed to be practically impossible with an ordinary computer. By comparison, a quantum computer could solve this problem very quickly [2]. This ability would allow a quantum computer to break many of the cryptographic systems in use today. It comes with no surprise that quantum computers could also

be useful for running simulations of many-body quantum systems [3, 4, 5, 6, 7]. In theory, these problems can be easily emulated with a well controlled quantum system. To reach a practical improvement, quantum algorithms require precise control in a large Hilbert space, making physical implementations difficult.

Recently, much attention has been focused on lattice gas algorithms as candidate quantum algorithms. Quantum lattice gas algorithms are the generalizations of classical lattice gas algorithms, which are implemented on a lattice of many identical simple units associated with homogeneous update rules to all the lattice sites. Such an architecture offers the experimental simplification that the early quantum hardware is likely to build in a similar manner.

Two types of quantum lattice gas algorithms are defined according to the quantum computing architectures: type-I and type-II quantum information processors. In a type-I design [8, 9, 10], the lattice points are presented by either the states of the quantum system or quantum qubits. The system wave function must remain coherent for the duration of the quantum gate sequence needed to implement a particular algorithm. An algorithm of type-I quantum lattice gas models unfolds the quantum operator into an ordered sequence of basic two-qubit quantum operations. Type-II [11] is essentially an array of small quantum information processors interconnected by classical communication channels. Quantum coherence only exist inside each processor for a short period. This particular architecture significantly simplifies the quantum controls by using magnetic resonance imaging (MRI) techniques. It may also increase the range of problems that small quantum processors can tackle and thus serve as an intermediate architecture between few-qubit and large scale quantum computers.

In the present thesis, I aim to provide a reader who is unfamiliar with the field of lattice gases and quantum lattice gases with an introduction to the lattice Boltzmann methods and recently progress in the quantum lattice gas algorithms. This thesis is divided into a comprehensive introduction which gives a detailed overview of lattice Boltzmann methods, followed by sections on the methodologies used to implement type-II quantum lattice gas algorithms using NMR. The approaches for improving the control and reducing errors during the experiments will be discussed in depth

in Chapter 4 and 5. In the last chapter, a brief introduction of type-I lattice gas algorithms is given and a preliminary experimental design using nuclear magnetic resonance (NMR) is presented.

Chapter 2

Type-II Quantum Lattice Gas Algorithm

2.1 Lattice Gas Method

The lattice gas method is a tool of computational physics used to model complex hydro-dynamical flows that are too large for a standard low-level molecular dynamics treatment. This method contains discontinuous inter-facial boundaries that prevent a high-level partial differential equation description [12, 13, 14, 15]. The basic idea underlying the lattice gas method is to statistically represent a macroscopic scale time-dependent field quantities by "averaging" repeated artificial microscopic particles scattering and propagating throughout a lattice of interconnected sites. Many particles are distributed over the lattice sites. These particles may coexist at each site at a given time, and each particle carries a unit mass and a unit momentum of energy. They interact on site by an artificial collision rule which is locally invariant under the point-group symmetries of the lattice, and, furthermore, which exactly conserves the total mass, momentum, and energy at that site. The movement of particles along the lattice is prescribed by a streaming operation that shifts particles to the nearest neighboring sites, thus endowing the particles with the property of momentum. In a

[1]This section was extracted from M. A. Pravia, Z. Chen, J. Yepez, D. G. Cory, "Experimental Demonstration of Quantum Lattice Gas Computation," QIP, 2002.

maximally discrete way, the algorithm encapsulates the microscopic scale kinematics of the particles scattering on site and moving along the lattice. The mean-free path length between collisions is about one lattice cell size, and the mean-free time between collision elapses after a single update. This is computationally simple in comparison to molecular dynamics where many thousands of updates are required to capture such particle interactions.

The mesoscopic evolution is obtained by taking the ensemble average over many steps in microscopic realization. At the mesoscopic scale, the average presence of each particle type is defined by a real-valued occupation probability. In addition, the microscopic collision and streaming rules translate into the language of kinetic theory. The behavior of the system is described by a transport equation for the occupation probabilities, and this equation is a discrete Boltzmann equation called the *lattice Boltzmann equation.*

The lattice Boltzmann equation further translates into a macroscopic, continuous, effective field theory by letting the cell size approach zero (the limit of infinite lattice resolution called the *continuum limit*). At the macroscopic scale, partial differential equations describe the evolution of the field, admitting solutions such as propagating sound wave modes and diffusive modes. The passage of the Boltzmann equation to the effective field theory begins by expanding the occupation probabilities, which have a well-defined statistical functional form in terms of the continuous macroscopic variables, such as the mass density ρ (and the velocity or energy field if they are defined in the model). This expansion usually is carried out perturbatively in a small parameter such as the Knudsen number (ratio of mean-free path to the largest characteristic length scale) or the Mach number (ratio of the sound speed to the largest characteristic flow speed) in a fashion analogous to the Chapman-Enskog expansion of kinetic theory. Conversely, the macroscopic field quantities can also be expressed as a function of the mesoscopic occupation probabilities–for example, the mass density at some point is a sum over the occupation probabilities in that vicinity.

2.2 The 1-D Diffusion Automaton

2.2.1 Microscopic Regime

We here consider a one-dimensional system [16, 17] in which particles may travel upwards or downwards to the nearest sites with some probabilities. Usually, a random walk is simulated by selecting one particle in the system and transporting it at random upwards or downwards, provided that the destination site is empty. At each site z of the lattice, we define two Boolean variables $n_1(z,t)$ and $n_2(z,t)$. These quantities are occupation numbers indicating whether or not a particle is entering site z at time t in direction e_1 (up) and e_2 (down), respectively.

In the microscopic regime, random motion is obtained by shuffling the two directions of motion indecently at each lattice site and at each time step. In other words, what is traveling in direction e_1 will be exchanged with what is traveling in direction e_2 with a probability $1-\mu(z,t)$. The micro-dynamics has two phases: collision and propagation to the nearest neighbor. A particle entering site $z+\Delta z$ at time $t+\Delta t$ with velocity pointing upwards must have been at site z at t. With a probability $\mu(z,t)$, this particle was the one with a velocity pointing upwards and with probability $1-\mu(z,t)$ the one which had a velocity pointing downwards. Therefore, the random walk rule obeys

$$\begin{aligned} n_1(z+\Delta z, t+\Delta t) &= \mu(z,t)n_1(z,t) + (1-\mu(z,t))n_2(z,t) \\ n_2(z-\Delta z, t+\Delta t) &= (1-\mu(z,t))n_1(z,t) + \mu(z,t)n_2(z,t). \end{aligned} \tag{2.1}$$

The time step is denoted by Δt, while the lattice spacing is given by Δz.

2.2.2 Mesoscopic Regime

At a mesoscopic scale, the variables n_i no longer appear as Boolean quantities but rather as an ensemble average of all the Boolean quantities (varying continuously between 0 and 1). Indeed, a mesoscopic point of coordinate z designates a microscopic volume comprising many particles. Formally, this averaging $f_i(z,t) =< n_i(z,t >$ is

treated as an ensemble average in the sense of statistical mechanics. Since $\mu(z,t)$ is statistically independent of $n_i(z,t)$, the average of $< \mu n_i >$ yields

$$< \mu(z,t)n_i(z,t) >=< \mu(z,t) >< n_i(z,t) >= pf_i(z,t). \tag{2.2}$$

The variables $f_1(z,t)$ and $f_2(z,t)$ are the occupation probabilities for finding upward- and downward-moving particles, respectively, at the site location z and time t. Therefore, relations in Eq. 2.1 can be averaged and yield

$$\begin{aligned} f_1(z+\Delta z, t+\Delta t) &= pf_1(z,t) + (1-p)f_2(z,t) \\ f_2(z-\Delta z, t+\Delta t) &= (1-p)f_1(z,t) + pf_2(z,t). \end{aligned} \tag{2.3}$$

In this case, the interesting quantity of the lattice gas is the mass density field, ρ, defines as the sum of upward- and downward-moving particles

$$\rho(z,t) = \sum_{i=1}^{2} f_i(z,t). \tag{2.4}$$

We can arrange Eq. 2.3 as following:

$$\begin{aligned} f_1(z+\Delta z, t+\Delta t) - f_1(z,t) &= (p-1)\left[f_1(z,t) - f_2(z,t)\right] \\ f_2(z-\Delta z, t+\Delta t) - f_2(z,t) &= (p-1)\left[f_2(z,t) - f_1(z,t)\right] \end{aligned} \tag{2.5}$$

By summing these two equations, we obtain

$$f_1(z+\Delta z, t+\Delta t) + f_2(z-\Delta z, t+\Delta t) - \rho(z,t) = 0. \tag{2.6}$$

This equation reflects the conservation of mass: the number of particles entering site z at time t are exiting at time $t+\Delta t$. For this reason, Eq. 2.6 is called the *continuity* equation.

The lattice gas described above is summarized by the Boltzmann equation

$$f_{1,2}(z \pm \Delta z, t + \Delta t) = f_{1,2}(z,t) + \Omega_{1,2}(z,t), \tag{2.7}$$

where the left-hand side denotes the occupation of the lattice as a function of the previous lattice configuration and where the collision terms are

$$\Omega_{1,2} = \pm(p-1)\left[f_1 - f_2\right] \tag{2.8}$$

The collision terms define different numerical problem that we desired to solve. It changes the direction of some particles, thus it is responsible for the diffusive behavior.

2.2.3 Macroscopic Regime

The Chapman-Enskog expansion technique is commonly used in statistical mechanics to derive the macroscopic laws governing the relevant physical quantities. The idea of the Chapman-Enskog expansion is the following: it is assumed that the actual occupation numbers f_i are close to the equilibrium population $f_i^{(0)}$. The occupation number can be expanded in terms of a small parameter ϵ:

$$f_i = f_i^{(0)} + \epsilon f_i^{(1)} + \epsilon^2 f_i^{(2)} + O(\epsilon^3), \tag{2.9}$$

where the $f_i^{(l)}$s are functions of z and t to be determined.

The next step is to take a Taylor expansion of the left-hand side of Eq. 2.5. One has

$$\begin{aligned} &f_i(z + \Delta z c_i, t + \Delta t) - f_i(z,t) = \\ &\left[\Delta t \partial_t + \frac{\Delta t^2}{2}\partial_t^2 + \Delta z c_i \partial_z + \frac{\Delta z^2}{2} c_i^2 \partial_r^2 + \Delta t \Delta z c_i \partial_t \partial_r\right] f_i(z,t), \end{aligned} \tag{2.10}$$

where we have defined $c_1 = -c_2 = 1$ and neglected third-order terms in the expansion. The infinitely short time step Δt and small lattice spacing Δz are not in the same order of magnitude when they approach the continuous limit. The propagation speed

v of the particles appears as the ratio between the lattice spacing and time step $\Delta z/\Delta t$, which remains finite. It turns out that the time step goes faster to zero than the lattice spacing because of an interesting case $(\Delta z)^2/\Delta t \rightarrow constant$. As a result, we express $\Delta z \sim \epsilon \Delta z$ and $\Delta t \sim \epsilon^2 \Delta t$.

By comparing both sides of Eq. 2.5 and Eq. 2.10, order by order,

$$\left[\Delta t\partial_t + \frac{\Delta t^2}{2}\partial_t^2 + \Delta z c_i \partial_z + \frac{\Delta z^2}{2} c_i^2 \partial_r^2 + \Delta t \Delta z c_i \partial_t \partial_r\right] f_i(z,t) \qquad (2.11)$$
$$= (1-p)\left[f_i(z,t) - f_j(z,t)\right],$$

we can obtain the solutions for $f_i^{(0)}$ and higher order terms as well. For the order $O(\epsilon^0)$ we have $f_1^{(0)}(z,t) = f_2^{(0)}(z,t)$ because the left-hand term is zero. This results in

$$f_1^{(0)} = f_2^{(0)} = \frac{1}{2}\rho \qquad (2.12)$$

and the condition that

$$\sum_{i=1}^{2} f_i^{(l)} = 0, if l \geq 1. \qquad (2.13)$$

The next order $O(\epsilon)$ of the Boltzmann equation is given by taking the term $\Delta z c_i \partial_z f_i^{(0)}$ of the Taylor expansion and the term $f_i^{(1)}$ in the right-hand side of the equation. Since $f_i^{(0)} = \rho/2$, we obtain

$$\frac{\Delta z}{2}\partial_z \rho = (p-1)(f_1^{(1)} - f_2^{(1)})$$
$$-\frac{\Delta z}{2}\partial_z \rho = (p-1)(f_2^{(1)} - f_1^{(1)}). \qquad (2.14)$$

The solution of Eq. 2.14 is then straightforward

$$f_i^{(1)} = \frac{\Delta z}{4(p-1)} c_i \partial_z \rho. \qquad (2.15)$$

The equation governing the evolution of ρ is given by the continuity Eq. 2.6. The order $O(\epsilon^1)$ reads

$$\sum_{i=1}^{2} \Delta z c_i \partial_z f_i^{(0)} = 0, \qquad (2.16)$$

which is obviously satisfied by our solution. The next order is $O(\epsilon^2)$

$$\sum_{i=1}^{2}\left[\Delta t\partial_t f_i^{(0)} + \Delta z c_i \partial_z f_i^{(1)} + \frac{\Delta z^2}{2} c_i^2 \partial_z^2 f_i^{(0)}\right] = 0. \tag{2.17}$$

Using the solution for $f_i^{(0)}$ and $f_i^{(1)}$, we obtain the equation

$$\partial_t \rho + \frac{\Delta z^2}{2}\left[\frac{1}{2(p-1)} + \frac{1}{2}\right]\partial_z^2 \rho = 0 \tag{2.18}$$

and, finally

$$\partial_z \rho = D\partial_z^2 \rho \tag{2.19}$$

which is the expected diffusion equation with the diffusion constant

$$D = \frac{\Delta z^2}{\Delta t}\frac{p}{2(1-p).} \tag{2.20}$$

Finally, in this implementation we consider an initial mass density $\rho(z, t = 0)$ whose evolution obeys the periodic boundary condition $\rho(z, t) = \rho(z + L, t)$, where L is the length of the lattice. As a result, the initial mass density diffuses until the total mass is evenly dispersed throughout the lattice.

2.2.4 Transition Matrix

We introduce a *transition matrix* $A(i, i')$, which gives the probability for an input state i transformed into an output state i' in a collision process. Clearly the whole collision process can be defined by giving the full transition matrix A. $A(i, i')$ obviously has

$$\sum_{i'} A(i, i') = 1 \tag{2.21}$$

for any i (This is the normalization constraint.). In some models, the transition matrix is symmetric:

$$A(i, i') = A(i', i) \tag{2.22}$$

and one says that *detailed balance* holds. However, in general, this is not true. A weaker property is the so-called *semi-detailed balance* which only requires

$$\sum_{i'} A(i, i') = 1 \tag{2.23}$$

for any i'. Semi-detailed balance is obeyed by most lattice gas models. The matrix that satisfies the normalization but does not hold detailed balance constraint is Markov or stochastic matrix. Satisfying both the normalization and semi-detailed balance, the matrix is referred as a doubly stochastic matrix.

2.3 Type-II Quantum Lattice Gas Algorithm

Quantum lattice gas (QLG) algorithms are generalizations of the classical lattice gas algorithms described above, where quantum bits are used to encode the occupation probabilities and where the principle of quantum mechanical superposition is added to the artificial microscopic world. In this quantum case, the mesoscopic occupation probabilities are mapped onto the wave functions of quantum mechanical sites. In the case where the quantum lattice gas describes a hydrodynamic system when the time evolution of the flow field is required, we must periodically measure these occupation probabilities, making the quantum lattice gas algorithm suitable to a type-II implementation. Such type-II algorithms have been shown to solve dynamical equations such as the diffusion equation [18], the Burgers equation [19], and magneto-hydrodynamic Burgers turbulence equation[20]. In this chapter, I will discuss about the QLG algorithm for the diffusion equation.

The quantum lattice gas algorithm that solves the 1-D diffusion equation derives from a classical lattice gas of particles moving up and down a 1-D lattice[18]. The corresponding quantum lattice gas algorithm description begins by encoding the occupation probabilities, and thus the mass density, in the states of a lattice of quantum objects. The streaming and collision operations are then a combination of classical and quantum operations, including measurements. The aim of the algorithm is to

take an initial mass density field and to evolve its underlying occupation probabilities according to the Boltzmann equation (2.7). A schematic of the entire quantum algorithm is shown in Fig. 3-3. A single time step of the algorithm is decomposed into four sequential operations:

1. encoding of the mass density
2. applying the collision operator $\hat{C}$ at all sites
3. measuring the occupation numbers
4. streaming to neighboring sites.

These operations are repeated until the mass density field has evolved for the desired number of time steps. In the first time step, the encoding operation specifies the initial mass density profile, while in all the subsequent steps the encoding writes the results of the previous streaming operation. The final time step ends with the readout of the desired result, so operation 4 is not performed.

Each occupation probability is represented as the quantum mechanical expectation value of finding a two-level system, or qubit, in its excited state $|1\rangle$. As a result, the state of the qubit encoding the value $f_i(z,t)$ is

$$|f_i(z,t)\rangle = \sqrt{f_i(z,t)}|1\rangle + \sqrt{1-f_i(z,t)}|0\rangle. \tag{2.24}$$

It follows that a single value of the mass density is recorded in two qubits, one for each occupation number. The combined two-qubit wave function for a single node becomes

$$\begin{aligned} |\psi(z,t)\rangle \;=\; & \sqrt{f_1 f_2}|11\rangle + \sqrt{f_1(1-f_2)}|10\rangle + \\ & \sqrt{(1-f_1)f_2}|01\rangle + \sqrt{(1-f_1)(1-f_2)}|00\rangle. \end{aligned} \tag{2.25}$$

The kets $|00\rangle$, $|01\rangle$, $|10\rangle$, and $|11\rangle$ span the joint Hilbert space of the two qubits, and this is the largest dimension space over which quantum superpositions are allowed. As with the classical algorithm, the constraint for local equilibrium (2.12) forces the

initial occupation probabilities at a node to be half of the corresponding mass density value.

The occupation numbers encoded in the two-qubit wave function $|\psi(z,t)\rangle$ can be recovered by measuring the expectation value of the number operator $\hat{n}_i$, as given in

$$f_i(z,t) = \langle\psi(z,t)|\hat{n}_i|\psi(z,t)\rangle, \tag{2.26}$$

where $\hat{n}_1 = \hat{n} \otimes \mathbf{1}$, $\hat{n}_2 = \mathbf{1} \otimes \hat{n}$, where $\mathbf{1}$ is the 2×2 identity matrix, and where the action of the single-qubit number operator $\hat{n}$ returns 1 if the qubit is in its excited state and 0 for the ground state.

The encoded occupation probabilities evolve as specified in the Boltzmann equation by the combined action of the collision operator, the measurement, and streaming. The collision operator contributes by taking the local average of the two occupation probabilities. This averaging (not to be confused with statistical coarse-grain averaging, time averaging, or ensemble averaging) is done by choosing the the collision operator $\hat{C}$ to be the "square-root-of-swap" gate, written as

$$\hat{C} = \begin{pmatrix} 1 & 0 & 0 & 0 \\ 0 & \frac{1+i}{2} & \frac{1-i}{2} & 0 \\ 0 & \frac{1-i}{2} & \frac{1+i}{2} & 0 \\ 0 & 0 & 0 & 1 \end{pmatrix} \tag{2.27}$$

in the standard basis. The propagator $\hat{C}$ induces local quantum entanglement. The same collision is applied simultaneously at every site, resulting in

$$|\psi'(z,t)\rangle = \hat{C}|\psi(z,t)\rangle \tag{2.28}$$

Using (2.26), the intermediate occupation probabilities of the wave function $|\psi'(z,t)\rangle$ are

$$f_i'(z,t) = \frac{1}{2}(f_1 + f_2) \tag{2.29}$$

as required for $i = 1, 2$. The third operation physically measures these intermediate

occupation probabilities $f_i'(z,t)$ at all the sites. A single time step is completed with the streaming of the occupation probabilities to the nearest neighbors, according to the rule

$$f_1(z-\Delta z, t+\Delta t) = f_1'(z,t) \tag{2.30}$$

$$f_2(z+\Delta z, t+\Delta t) = f_2'(z,t). \tag{2.31}$$

The information of each qubit is shifted to the neighboring sites in opposite directions. The streaming operation is a classical step causing global data shifting, and it is carried out in a classical computer interfaced to the quantum processors. Together, the last three operations result in

$$f_{1,2}(z \pm \Delta z, t+\Delta t) = \frac{1}{2}\left[f_1(z,t) + f_2(z,t)\right], \tag{2.32}$$

which is the exact dynamics described by the Boltzmann equation (2.7).

Chapter 3

NMR Demonstration

Here, we explore the experimental aspects of building a type-II quantum computer using NMR techniques [21]. QIP experiments utilizing NMR typically employ a liquid sample of molecules containing spin-$\frac{1}{2}$ nuclei. The sample is subjected to a strong magnetic field B_0 of order $\sim$ 10 T creating an energy difference ΔE between the aligned and anti-aligned spin states that results in an equilibrium state with net magnetization. At room temperature, $\Delta E/k_B T$ is about 10^{-5}, so that the net magnetization is relatively small, but, given the large number of molecules in the sample ($\sim 10^{18}$), it is still easily detectable. The entire spin ensemble is accurately described by a reduced density matrix of only the intramolecular spin degrees of freedom. The ensemble nature of the NMR sample thus makes it inherently applicable to parallel computation. A type-II architecture can be mapped onto an NMR sample by creating a correspondence between the sites of the lattice and spatially distinct spin ensembles. Using magnetic field gradients and radio frequency (RF) pulses, information in the lattice can be encoded, manipulated, and read out.

[1]This section was extracted from M. A. Pravia, Z. Chen, J. Yepez, D. G. Cory, "Experimental Demonstration of Quantum Lattice Gas Computation," QIP, 2002.

3.1 Methodology for NMR Implementations

3.1.1 Spin System and Control

For this two-qubit problem, we chose a room-temperature solution of isotropically-labeled chloroform ($^{13}CHCl_3$), where the hydrogen nucleus and the labeled carbon nucleus served as qubits 1 and 2 Fig. 3-1, respectively. The chloroform sample was divided into 16 classically-connected sites of two qubits each, creating an accessible Hilbert space larger than would be available with 32 non-interacting qubits.

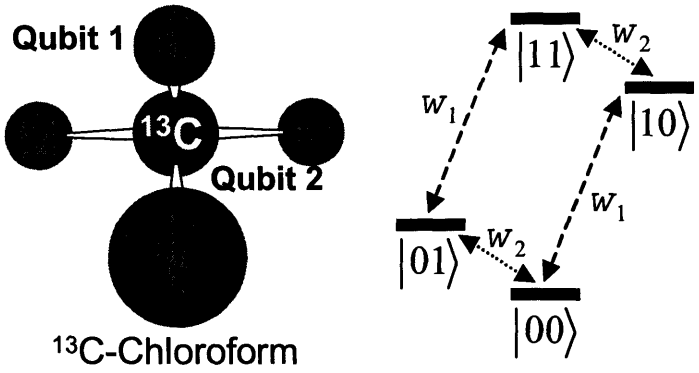

Figure 3-1: **Labeled chloroform** Labeled chloroform consists of two qubits, the hydrogen nucleus and labeled carbon served as qubits 1 and 2. States $|0\rangle$ and $|1\rangle$ are the ground state and excited state, respectively, induced by the Zeeman interaction with the applied magnetic field. Frequencies w_1 and w_2, defined as multiplication of the gyro-magnetic ratio γ and the magnetic field B_0, are the resonant frequencies to flip the spins.

The internal Hamiltonian of this system in a strong and homogeneous magnetic field B_0 is

$$H_{internal} = -\frac{1}{2}\left(\gamma_H B_0\right)\sigma_z^1 - \frac{1}{2}\left(\gamma_C B_0\right)\sigma_z^2 + \frac{\pi J}{2}\sigma_z^1\sigma_z^2 \tag{3.1}$$

where the first two terms represent the Zeeman couplings of the spins with B_0 and the last term is the scalar coupling between the two spins. The operators of the form σ_k^i are Pauli spin operators for the spin i and the Cartesian direction k. In the rotating frame, the internal Hamiltonian can be reformulated as: $H_{internal} = \frac{\pi J}{2}\sigma_z^1\sigma_z^2$. The choice of chloroform is particularly convenient because the different gyro-magnetic ratios, γ_H

and γ_C, generate widely spaced resonant frequencies. As a result, a RF pulse applied on resonance with one of the spins does not affect, to a good approximation, the other spin. In the 7 T magnet utilized for the implementation, the hydrogen and carbon frequencies were about 300 MHz and 75 MHz, respectively. The widely spaced frequencies allow us to write the two RF control Hamiltonians as acting on the two spins independently. More concretely, the externally-controlled RF Hamiltonians are written as

$$H^i_{RF}(t) = -\frac{1}{2}\left[w^i_x(t)\sigma^i_x + w^i_y(t)\sigma^i_y\right] \tag{3.2}$$

The RF Hamiltonians generate arbitrary single-spin rotations with high fidelity when the total nutation frequencies

$$\nu^i_{RF} = \frac{1}{2\pi}\sqrt{[w^i_x]^2 + [w^i_y]^2} \tag{3.3}$$

are much stronger than J, the scalar coupling constant. The scalar coupling Hamiltonian and the single-spin rotations permit the implementation of a universal set of gates, and they are the building blocks for constructing more involved gates such as the collision operator $\hat{C}$.

The lattice of quantum information processors shown in Fig. 3-2 is realized by superimposing a linear magnetic field gradient on the main field B_0, adding a position dependent term to the Hamiltonian having the form

$$H_{gradient}(z) = -\frac{1}{2}\left(\gamma_H \frac{\partial B_z}{\partial z} z\right)\sigma^1_z - \frac{1}{2}\left(\gamma_C \frac{\partial B_z}{\partial z} z\right)\sigma^2_z \tag{3.4}$$

The variable z denotes the spatial location along the direction of the main field, while the constant $\frac{\partial B_z}{\partial z}$ specifies the strength of the gradient. The usefulness of this Hamiltonian can be appreciated by noticing that the offset frequencies $\Delta\Omega_{H,C} = \gamma_{H,C}\left(\frac{\partial B_z}{\partial z}\right) z$ of the spins vary with position when the gradient field is applied. Spins at distinct locations can thus be addressed with RF fields oscillating at the corresponding frequencies. In this way, the magnetic field gradient allows the entire spin ensemble to be sliced into a lattice of smaller, individually addressable sub-ensembles.

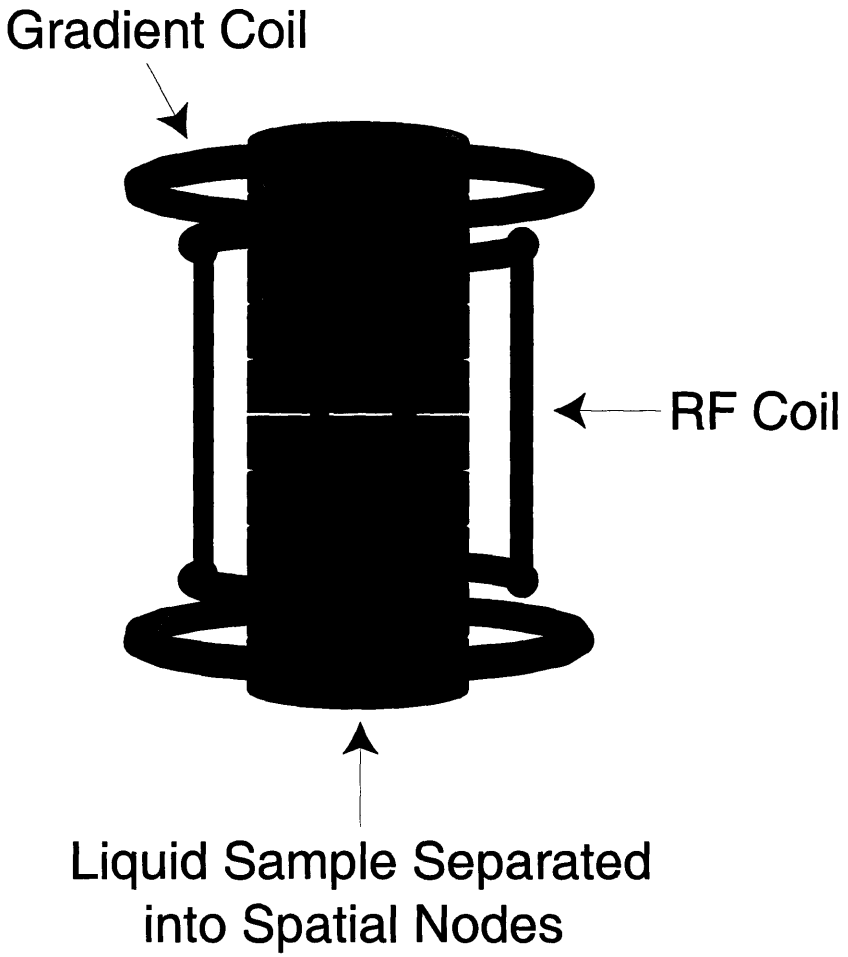

Figure 3-2: **Liquid sample in the coils** The lattice initialization is demonstrated. The liquid sample is placed in the middle with the gradient coils on both ends and surrounded by the RF coils. Once the gradient field is turned on, the resonant frequencies across the sample will vary corresponding to the strength and duration of the gradient. Thus, the spin ensemble can be sliced into a lattice of small blocks.

Using the coupling, RF, and gradient Hamiltonians described above, together with the appropriate measurement and processing tools, we can now describe in detail how the four steps of the diffusion QLG algorithm translate to experimental tasks. The lattice initialization step (1) uses the magnetic field gradients to establish sub-ensembles of varying resonant frequency addressable with the RF Hamiltonians as described in Fig. 3-3. The collision step (2) makes use of both the RF and the internal coupling Hamiltonians to generate the desired unitary operation $\hat{C}$. The readout (3) is accomplished by measuring the spins in the presence of a magnetic field gradient. And finally, the streaming operation (4) is performed as a processing step in a classical computer in conjunction with the next initialization step.

3.1.2 Lattice Initialization

The initialization of the lattice begins by transforming the equilibrium state of the ensemble into a starting state amenable for quantum computation. At thermal equilibrium, the density matrix is

$$\sigma_{thermal} = \frac{1}{\mathcal{Z}} \exp\left[-\frac{H_{internal}}{k_B T}\right] \approx \frac{\mathbf{1}}{2^2} + \epsilon \left[\frac{\gamma_H}{\gamma_C}\sigma_z^1 + \sigma_z^2\right], \tag{3.5}$$

where ϵ has a value on the order of 10^{-5} and $\mathcal{Z}$ is the partition function. The equilibrium state is highly mixed and the two spins have unequal magnetizations. To perform quantum computations, it is convenient to transform the equilibrium state into a pseudo-pure state [22, 23], a mixed state whose deviation part transforms identically to the corresponding pure state and, when measured, returns expectation values proportional to those that would be obtained by measuring the underlying pure state. Two transformations create the starting pseudo-pure state $|00\rangle$ from the thermal state. First, the magnetizations of the two spins are equalized [2], illustrated

[2]This is achieved by applying the pulse sequence: $\left[\frac{\pi}{2}\right]_x^{H,C} \rightarrow \left(\frac{1}{4J}\right) \rightarrow \left[\frac{\pi}{2}\right]_y^{H,C} \rightarrow \left(\frac{1}{4J}\right) \rightarrow \left[\frac{\pi}{2}\right]_{-x}^{H,C} \rightarrow gradient(z)$.

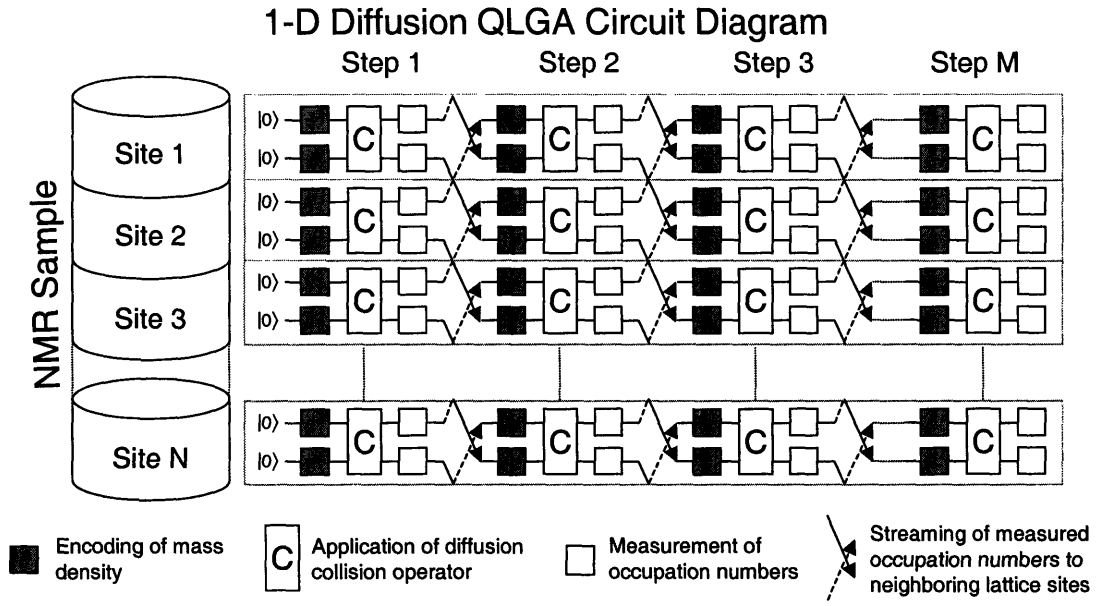

Figure 3-3: **Quantum lattice gas algorithm for solving the 1-D diffusion equation.** The algorithm employs N two-qubit sites to encode the discretized mass density. Each site codes for a single value of the mass density using the quantum state of the two qubits. The encoded information is subjected to a series of local transformations that evolve the system. The collision operator C is the only entangling operation in the algorithm, and it creates quantum coherences limited to each two-qubit system. The streaming is executed by classical communication, and it moves the occupation numbers up and down the lattice as denoted by the arrows. The sectioned cylinder depicts the position of the sites in the NMR sample. Each site is physically realized as an addressable slice of isotropically-labeled chloroform solution.

in Fig. 3.1.2,

$$\sigma_{thermal} \overset{Equalize}{\longrightarrow} \sigma_{equal} = \frac{\mathbf{1}}{2^2} + \frac{\epsilon}{2}\left(1 + \frac{\gamma_H}{\gamma_C}\right)\left[\sigma_z^1 + \sigma_z^2\right] \tag{3.6}$$

followed by a pseudo-pure state creation sequence [3] that results in

$$\sigma_{equal} \overset{Pseudo-pure}{\longrightarrow} \sigma_{pp} = \frac{\mathbf{1}}{2^2} + \epsilon\frac{\sqrt{3}}{4\sqrt{2}}\left(1 + \frac{\gamma_H}{\gamma_C}\right)\left[\sigma_z^1 + \sigma_z^2 + \sigma_z^1\sigma_z^2\right]. \tag{3.7}$$

The equalization and pseudo-pure state creation sequences are described in detail in reference [24]. For clarity, we define the constant in front of the brackets to be ϵ', allowing us to write the pseudo-pure state σ_{pp} in terms of the desired spinor $|00\rangle$ as

$$\sigma_{pp} = \left(\frac{1}{4} - \epsilon'\right)\mathbf{1} + \epsilon'|00\rangle\langle 00|. \tag{3.8}$$

Expressed in this manner, it is now more easily seen how a unitary transformation applied to σ_{pp} acts trivially on the term proportional to the identity, but it evolves the term $|00\rangle\langle 00|$ as it would a pure state as shown in Fig. 3-5.

Individually addressing the sites of the lattice, as depicted in Fig. 3-3, is accomplished by selectively addressing slices of the cylindrical sample. The procedure is related to slice-selection in magnetic resonance imaging (MRI) [25], and it works by applying the gradient Hamiltonian in the presence of suitably shaped RF pulses. First, consider the Hamiltonian for a one-spin system subjected to a linear magnetic field gradient in the z-direction and to a time-dependent RF pulse applied in the y-direction. In this case, the Hamiltonian is

$$H_{RF,G}(z,t) = -\frac{1}{2}\left(\gamma\frac{\partial B_z}{\partial z}z\right)\sigma_z - \frac{1}{2}w_y(t)\sigma_y \tag{3.9}$$

where the σ_z term is the linearly-varying static field and the σ_y term is the time-dependent RF. The Hamiltonian $H_{RF,G}(z,t)$ does not commute with itself at all times, so a closed-form and exact solution cannot be easily given without specifying the

[3] It is accomplished by the application of $\left[\frac{\pi}{4}\right]_x^{H,C} \rightarrow \left(\frac{1}{2J}\right) \rightarrow \left[\frac{\pi}{6}\right]_y^{H,C} \rightarrow gradient(z)$.

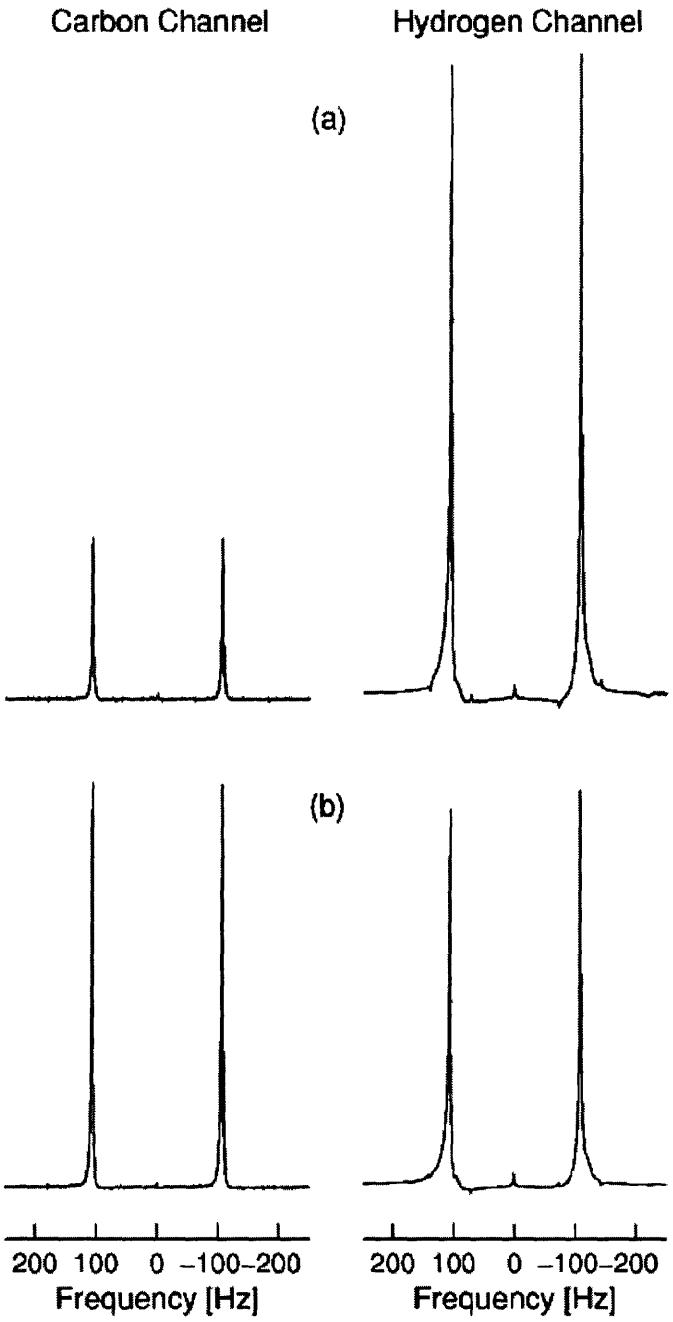

Figure 3-4: **Equalizing magnetization** Since the ratio of γ_H to γ_C is a factor of four, the spectra of H and C following a $\frac{\pi}{2}$ pulse should reflect 4 : 1 ratio in the peak heights, shown in (a). In order to compensate the different magnetization, the equalization pulse sequence is applied and results in the spectrum (b).

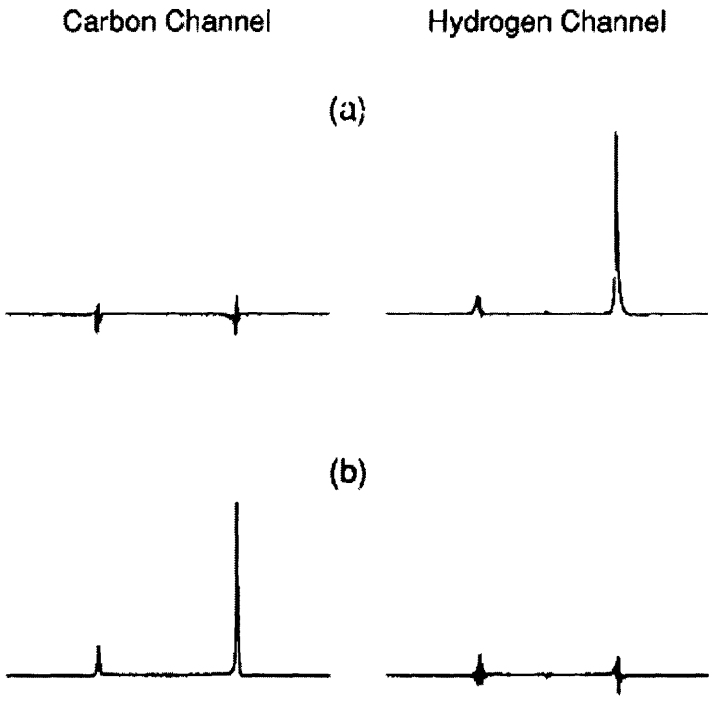

Figure 3-5: **Pseudo-pure states** The results of pseudo-pure states of hydrogen and carbon are shown in (a) and (b), respectively.

function $w_y(t)$. (The two terms in the Hamiltonian doesn't commute with each other at all times.) A valuable approach, however, is to consider the approximate evolution generated by $H_{RF,G}(z,t)$ during infinitesimal periods of the RF pulse. To first order, the evolution during the initial period Δt becomes

$$U_{RF,G}(z, t = \Delta t) \approx \exp\left[i\frac{1}{2}\left(\gamma\frac{\partial B_z}{\partial z}\Delta t\right) z\ \sigma_z\right] \exp\left[i\frac{w_y(\Delta t)\Delta t}{2}\sigma_y\right]. \tag{3.10}$$

By defining the term in the parenthesis as $\Delta k_z \equiv \gamma\frac{\partial B_z}{\partial z}\Delta t$, the evolution of an initial density matrix σ_z through a single period becomes

$$U_{RF,G}\sigma_z U_{RF,G}^{\dagger} \approx \exp\left[i\frac{\Delta k_z z}{2}\sigma_z\right]\sigma_x \exp\left[-i\frac{\Delta k_z z}{2}\sigma_z\right] w_y(\Delta t)\Delta t + \sigma_z \tag{3.11}$$

where small angle approximations have been made. The first term is a spatial helix

of the x and y magnetizations having a wavenumber Δk_z. The second term is the first order approximation to the magnetization remaining in the state σ_z. Another period of evolution will affect the σ_z term as described, creating a new magnetization helix with wavenumber Δk_z. In addition, the initial helix will have its wavenumber increased by an amount Δk_z. The final result over many periods is the formation a shaped magnetization profile having many components

$$\sigma_z \rightarrow \sum_{n=1}^{N} \exp\left[i\frac{n\Delta k_z z}{2}\sigma_z\right]\sigma_x \exp\left[-i\frac{n\Delta k_z z}{2}\sigma_z\right] w_y(n\Delta t)\Delta t + \sigma_z. \tag{3.12}$$

Each term in summation can be interpreted as a cylindrical Fourier component of the $x-y$ magnetization weighted by the RF nutation rate $w_y(n\Delta t)$. The RF waveform specifies the magnitude of each spatial Fourier component, and the resulting spatial profile is the Fourier transform of the RF waveform[30]. An equivalent description is to say that, for weak RF pulses, the excited magnetization of the spins at a given resonance frequency is, to first order, proportional to the Fourier component of the RF waveform at that frequency. As a result, control of the appropriate RF Fourier component essentially translates to selective addressing of spatial frequencies, which in turn allows the excitation of particular spatial locations.

The Fourier transform approximation allows encoding of arbitrary shapes on the various spatial locations of one uncoupled nuclear species. For QIP, however, coupled spins are required to implement entangling operations. In particular, the chloroform carbons and protons are coupled together via the scalar coupling. Given that the required RF waveforms should be weak, the coupling interferes with the desired evolution. The effect of the coupling present while encoding on spin 1 is removed by applying a strong RF decoupling sequence on the second spin [4]. The decoupling modulates the σ_z^2 operator in the interaction Hamiltonian, making its average over

[4]The decoupling was accomplished by applying the pulse cycle $Q\bar{Q}\bar{Q}Q$ during the positive and negative gradients. The element Q is a composite π pulse implemented with four sequential pulses having nutation angles $80.4°, 362.0°, 181.6°, 180.8°$ and respective phases $271.3°, 132.4°, 292.3°, 200.4°$. This composite pulse was chosen over more commonly used pulse sequences for its relatively short total nutation angle and good decoupling, allowing the cycle to fit within a gradient period.

a cycle period equal to zero. As a result, the second spin feels an identity operation during the decoupling. Fig. 3-6 shows the complete RF and gradient pulse sequence. As can be seen from the diagram, the first encoding on qubit 1 was subsequently swapped to qubit 2, followed by a re-encoding of qubit 1. We chose this method because the smaller gyro-magnetic ratio of ^{13}C causes a narrower frequency dispersion in the presence of the gradients, making the carbon decoupling simpler.

As described above, the encoding process writes the desired shapes in the spatial dependence of each spin's x-magnetization. The occupation numbers, however, are proportional to the z-magnetization, as can be seen when the number operator in the equation

$$f_i(n\Delta z, m\Delta t) = \langle\psi(n\Delta z, m\Delta t)|\hat{n}_i|\psi(n\Delta z, m\Delta t)\rangle, \tag{3.13}$$

is replaced with $\hat{n}_i = \frac{1}{2}(1 + \sigma_z^i)$ resulting in

$$f_i(n\Delta z, m\Delta t) = \frac{1}{2}\left[1 + \langle\psi(n\Delta z, m\Delta t)|\sigma_z^i|\psi(n\Delta z, m\Delta t)\rangle\right]. \tag{3.14}$$

where second term in the brackets represents the z-magnetization. The encoding process is followed by a $\pi/2$ pulse that rotates the excited x-magnetization to the z direction.

3.1.3 Collision and Swap Gates

After initialization, the next step is to apply the collision operator. For the QLG algorithm solution to the diffusion equation, the collision operator $\hat{C}$ is the square-root-of-swap gate. Expressed in terms of the Pauli operators, it is

$$\hat{C} = \exp\left[-i\frac{\pi}{8}\left(\sigma_x^1\sigma_x^2 + \sigma_y^1\sigma_y^2 + \sigma_z^1\sigma_z^2\right)\right] \tag{3.15}$$

where an irrelevant global phase has been ignored. Written in this form, the operation $\hat{C}$ can be decomposed into a sequence of implementable RF pulses and scalar coupling evolutions[33, 35] by noticing that the product operators in the exponent commute

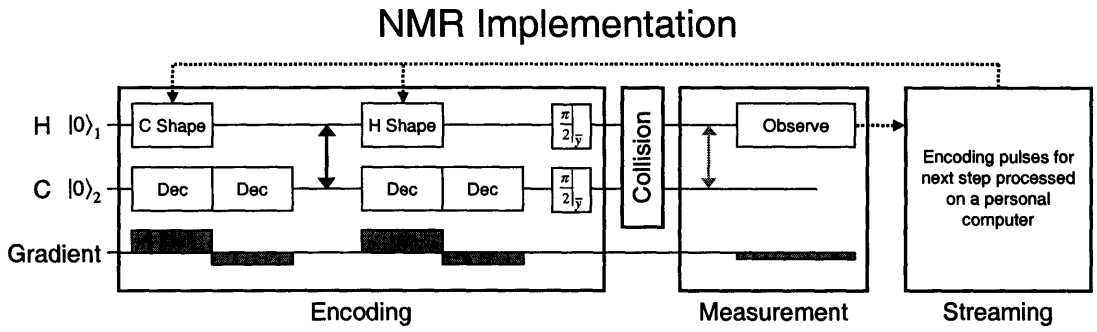

Figure 3-6: **NMR methodology for QLG algorithm.** The NMR implementation consists of four main sections, each corresponding to the prescribed QLG algorithm step. The top two lines in the diagram correspond to RF pulses applied to the proton and carbon qubits, respectively. The third line shows the application of magnetic field gradients. In the encoding section, the initial carbon magnetization is recorded on the protons before being transferred to the carbons. The starting magnetization is specified by using a RF pulse shaped as the Fourier transform of the desired magnetization. The shaped pulses are applied in the presence of gradients so that each site can be addressed. A carbon decoupling sequence prevents the scalar coupling from interfering with the low power shaped pulses. The $\frac{\pi}{2}$ at the end of the encoding move the information form the x-axis to the z-axis, as required by the QLG algorithm. The collision operator follows the encoding, and it is implemented without gradients to ensure that all of the sites in the sample feel the same transformation. The results are observed in two experiments, each time using the more sensitive proton channel. A swap gate is added when measuring the carbon magnetization. Finally, the streaming operation is applied by shifting the frequencies of the carbon and proton shapes in opposite directions.

with each other, resulting in

$$\hat{C} = \exp\left[-i\frac{\pi}{8}\sigma_y^1\sigma_y^2\right]\exp\left[-i\frac{\pi}{8}\sigma_z^1\sigma_z^2\right]\exp\left[-i\frac{\pi}{8}\sigma_x^1\sigma_x^2\right] \tag{3.16}$$

Expanding the first and last exponentials as scalar couplings sandwiched by the appropriate single-spin rotations results in

$$\begin{aligned}\hat{C} \;=\; & \exp\left[i\frac{\pi}{4}\sigma_x^1\right]\exp\left[i\frac{\pi}{4}\sigma_x^2\right]\exp\left[-i\frac{\pi}{8}\sigma_z^1\sigma_z^2\right]\exp\left[-i\frac{\pi}{4}\sigma_x^1\right]\exp\left[-i\frac{\pi}{4}\sigma_x^2\right]\cdot \\ & \exp\left[-i\frac{\pi}{8}\sigma_z^1\sigma_z^2\right]\cdot \\ & \exp\left[-i\frac{\pi}{4}\sigma_y^1\right]\exp\left[-i\frac{\pi}{4}\sigma_y^2\right]\exp\left[-i\frac{\pi}{8}\sigma_z^1\sigma_z^2\right]\exp\left[i\frac{\pi}{4}\sigma_y^1\right]\exp\left[i\frac{\pi}{4}\sigma_y^2\right]\end{aligned} \tag{3.17}$$

The exponents of terms proportional to $\sigma_z^1\sigma_z^2$ represent internal Hamiltonian evolutions lasting for a time $t_{zz}^{col} = 1/(4J)$. The exponents of terms with single-spin operators are implemented by $\pi/2$ rotations as in Fig. 3-7. They were generated by RF pulses whose nutation rate was about 50 times greater than J. All of the pulses and delays were applied without a magnetic field gradient in order to transform all of the sites identically.

As shown in Fig. 3-6, swap gates were utilized both in the lattice initialization and in the measurement of the carbon magnetization. The pulse sequence for the swap gates was almost identical to the sequence for $\hat{C}$. The only difference was that the internal evolution delay was set to $t_{zz}^{swap} = 1/(2J)$.

3.1.4 Measurement

If the algorithm is performed on individual quantum systems, then the values are obtained by averaging over many strong quantum measurements of identical instances of each step. However, when the algorithm is performed using a large ensemble of quantum systems, as in the case of NMR, then a single weak measurement of the entire ensemble can provide sufficient precision to obtain $f_i'(z,t)$. The occupation numbers resulting from the collision were obtained by measuring the z-magnetizations and using equation (3.14). Since only the σ_x^i and σ_y^i operators are directly observable,

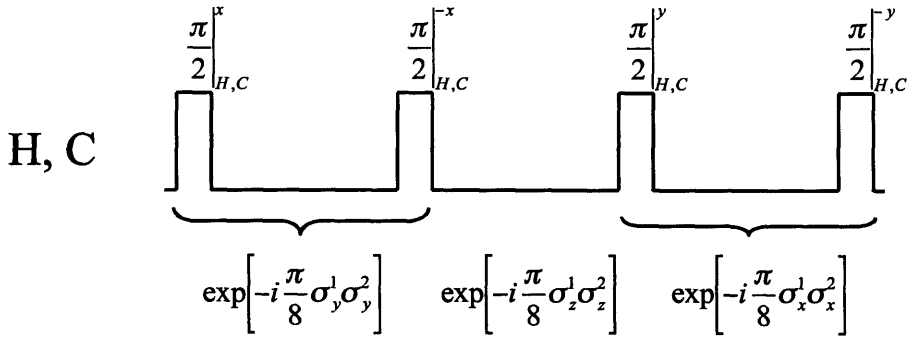

Figure 3-7: **Pulse sequence for the collision operator** The collision operator for the diffusion equation can be generated by applying $\frac{\pi}{2}$ pulses on both channels with delay time $\frac{1}{4J}$ in between. The same sequence can be used to generate the swap gate by increasing the delay time to $\frac{1}{2J}$.

a "read out" $\pi/2$ pulse transformed the z-magnetization into x-magnetization. The proton magnetization was measured directly after the collision, while the carbon magnetization was first swapped to the protons before observation. Measurements of both the ^{13}C and ^{1}H magnetizations were carried out separately, and in both cases via the more sensitive proton channel. The measurements were made in the presence of a weak linear magnetic field gradient, causing signals from different sites to resonate with distinguishable frequencies. The observed proton signal was digitized and Fourier transformed to record an image of the spatial variation of the spin magnetization. The observed spectrum was then processed to correct the baseline and to obtain the resulting magnetization at each site. Because each site is composed of a slice of the

sample with spins resonating in a band of frequencies, the occupation number for each site was obtained by averaging over all spins in the corresponding band.

3.1.5 Streaming

The final step involves classically streaming the results of the measurements according to Eqs. (2.30) and (2.31). For the diffusion equation, the streaming operation is applied in conjunction with the next lattice initialization step by adding a linearly varying phase to the Fourier transform of the desired shape. The added phase causes a shift in the frequency of the pulse determined by the slope of the phase. When the frequency-shifted pulse is applied in the presence of the magnetic field gradient, the shift results in spatial translation of the encoded shape. The streaming operation is thus implemented as a signal processing step in the lattice initialization procedure.

3.2 Experiment Demonstration

The results of the experiment are shown in Fig. 3-8, together with plots of the analytical solution and of numerical simulations of the NMR experiment. In total, 7 steps of the algorithm were completed using a parallel array of 16 two-qubit ensemble NMR quantum processors. The observed deviations between the data points and the analytical plots can be attributed to imperfections in the various parts of the NMR implementation.

3.3 Conclusion

Ensemble NMR techniques have been used to study the experimental details involved in quantum information processing. The astronomical number of individual quantum systems ($\sim 10^{18}$) present in typical liquid-state spin ensembles greatly facilitates the problem of measuring spin quantum coherences. In addition, the ensemble nature has been successfully utilized to create the necessary pseudo-pure states[22, 23] and to systematically generate non-unitary operations over the ensemble [26]. In this

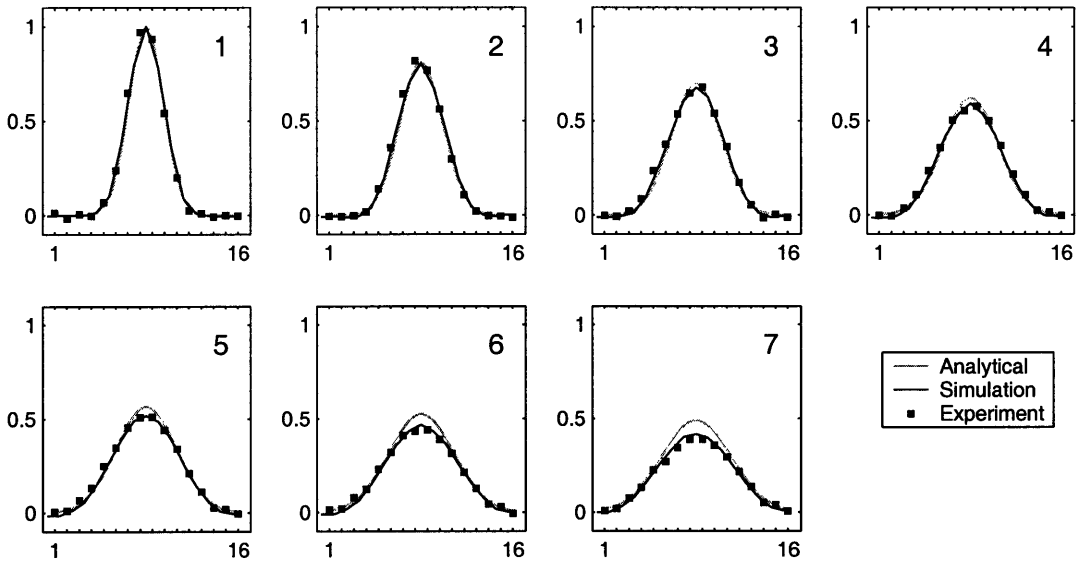

Figure 3-8: **QLG algorithm experimental results.** The experimental mass densities are plotted in the figure, together with plots of the analytical solution and the numerical simulation of the NMR experiment. Seven steps of the algorithm were implemented on 16 two-qubit sites. The simulations were performed using the actual RF nutation rates and times of the experimental setup. The calculations closely match the data, suggesting that the deviation between the analytical results and the data can be attributed imperfections in the methodology. As a result, the simulations promise to be useful in exploring the errors from alternate methods.

experiment, we again exploit the ensemble nature, but this time as a means of realizing a parallel array of quantum information processors. The novel architecture is then used to run a quantum lattice gas algorithm that solves the 1-D diffusion equation.

The closeness of the data to the analytical results is encouraging, and it demonstrates the possibility of combining the advantages of quantum computation at each node with massively parallel classical computation throughout the lattice. Currently, commercial MRI machines routinely take images with $256 \times 256 \times 256$ volume elements. As a result, the large size of the NMR ensemble provides, in principle, sufficient room to explore much larger lattices. However, in moving to implementations with more computational power, several challenges remain. The limited control employed here is sufficient for a few time steps of the algorithm, but refinements are necessary to increase the number of achievable iterations. In addition, although complicated op-

erations have been done in up to 7 NMR qubits [27, 28, 29], the problem of efficiently initializing a large lattice of few-qubit processors still remains. Our results provide a first advance in this direction, and they provide confirmation that NMR techniques can be used to test these new ideas.

Chapter 4

Systematic Error

The ensemble nature of the spin system allows us to split the sample into a spatial array of lattice sites. As we mentioned in the previous chapter, well developed methods from MRI [25] allow us to selectively address the spins in each of these sites. Typically the addressing is carried out in a space reciprocal to the spatial mapping, called k-space [30], where k is the wave-number of the corresponding Fourier components. The k-space formalism provides a recipe for writing a spatially varying spin rotation across an ensemble of spins that have been distinguished from each other by a magnetic field gradient. The k-space formalism is essentially the application of shaped RF pulses in the presence of a linear magnetic gradient field as a means of exciting selective frequencies. For most studies the full k-space formalism is not employed and a linear approximation is invoked. If the rotation angle of the shaped pulse is small, then the excited magnetization may be accurately calculated only to first order in that angle, and the excited magnetization is related to the RF waveform simply by a Fourier transform. As a result, the required RF waveform can also be determined by taking the inverse Fourier transform of the desired initial magnetization. This technique allows us to encode arbitrary magnetization profiles spanning the various spatial locations in our experiment and thereby approximating any desired initial conditions. In the previously implemented diffusion equation, higher order Fourier

[1]This section was extracted from Z. Chen, J. Yepez, D. G. Cory, "Simulation of the Burgers equation by NMR quantum information processing," submitted, 2005.

components of the number density are attenuated by the dynamics and the solution is stable even in the presence of substantial accumulated errors.

To push the development of type-II implementations we have chosen to explore the nonlinear Burgers equation to test the breakdown for the linear approximation. Over time, a shock front forms and high spatial frequencies in the magnetization profile become important and it is these high spatial frequencies that we expect to be most sensitive to errors. The numerical treatment of the QLG algorithm for the Burgers equation therefore offers a stronger proof of our NMR quantum computing approach since the effect of the nonlinear convective term in the equation generates a sharp edge as a shock develops in time that is not mimicked by spin relaxation, random self-diffusion, nor RF inhomogeneities.

4.1 The Burgers Equation

4.1.1 QLG Algorithm for the Burgers Equation

The QLG algorithm is initialized, in the NMR case, by encoding the particles' occupation probabilities as a spin-magnetization profile. To handle the one-dimensional Burgers equation [19], it is sufficient to use two qubits (two spin-$\frac{1}{2}$ nuclei) per lattice site, where each stores a single real valued occupation probability. A lattice of QIPs are related to the ensemble sample by creating a correspondence between lattice sites and spatially dependent positions in the sample. The dynamical evolution is caused by a collision operator (a quantum operation), and measurement and streaming (classical operations) according to the QLG algorithmic paradigm.

First, each occupation probability is mapped onto a lattice site as the expectation value of a number operator at a space time site z at time t. As a result, the initial state of the i^{th} qubit is $\sqrt{f_i(z,t)}|1\rangle + \sqrt{1-f_i(z,t)}|0\rangle$. The combined the wave function for a lattice site is a tensor product over the qubits:

$$|\psi\rangle = \sqrt{f_1 f_2}|11\rangle + \sqrt{f_1(1-f_2)}|10\rangle + \sqrt{(1-f_1)f_2}|01\rangle + \sqrt{(1-f_1)(1-f_2)}|00\rangle. \quad (4.1)$$

In the basis of a two-qubit system, the number operators for the occupancy of qubits are defined in terms of the single qubit number operation $\hat{n} = \begin{pmatrix} 1 & 0 \\ 0 & 0 \end{pmatrix}$ as follows: $\hat{n}_1 = \mathbf{1} \otimes \hat{n}$ and $\hat{n}_2 = \hat{n} \otimes \mathbf{1}$. Therefore, the occupation probability is represented as follows:

$$f_i(z,t) = \langle \psi(z,t) | \hat{n}_i | \psi(z,t) \rangle. \tag{4.2}$$

The macroscopic scale dynamical quantity of the quantum lattice gas is the number density, ρ, defined as the sum of the occupancy probability. The equilibrium occupation probabilities that we use are

$$\begin{aligned} f_1^{eq} &= \frac{\rho}{2} + \frac{1}{2\alpha}\sqrt{\alpha^2+1} - \frac{1}{2\alpha}\sqrt{(\alpha^2+1) - 2\alpha^2\rho + \alpha^2\rho^2} \\ f_2^{eq} &= \frac{\rho}{2} - \frac{1}{2\alpha}\sqrt{\alpha^2+1} + \frac{1}{2\alpha}\sqrt{(\alpha^2+1) - 2\alpha^2\rho + \alpha^2\rho^2}. \end{aligned} \tag{4.3}$$

where α is denoted by $\cot\theta\cos(\zeta - \xi)$ for convenience. (θ, ξ, and ζ are the "Euler" angles introduced by the collision operator, which will be covered below.)

Second, the evolution of f_i is governed by the combined action of the collision operator, measurement and streaming. The collision operator is applied to all the lattice sites independently, resulting in $|\psi'(z)\rangle = \hat{C}|\psi(z)\rangle$, for all lattice sites. The choice of the particular components of the unitary collision operator determines the form of the macroscopic effective field theory (a parabolic partial differential equation) and the value of its transport coefficients (coefficients of the dissipative terms). A general representation of the collision operator for the Burgers equation is a block diagonal matrix. This single quantum operator has the following matrix representation:

$$\hat{C} = \begin{pmatrix} 1 & 0 & 0 & 0 \\ 0 & e^{i\phi}e^{i\xi}\cos\theta & e^{i\phi}e^{i\zeta}\sin\theta & 0 \\ 0 & -e^{i\phi}e^{-i\zeta}\sin\theta & e^{i\phi}e^{-i\xi}\cos\theta & 0 \\ 0 & 0 & 0 & 1 \end{pmatrix}, \tag{4.4}$$

where ϕ, ξ, ζ, and θ are the "Euler" angles. The corresponding nonlinear Burgers

equation reads

$$\frac{\partial \rho}{\partial t} + c \sin 2\theta \cos(\zeta - \xi)\,(\rho - 1)\,\frac{\partial \rho}{\partial z} = \frac{1}{2}\frac{\Delta z}{\Delta t}\frac{\partial^2 \rho}{\partial z^2}. \tag{4.5}$$

Here, Δt is the update time and a cell size is presented by Δz. The propagation speed c of particles is determined as the ratio of the lattice cell size to the time step interval.

Third, we measure the occupation probabilities. This process erases all the superpositions and quantum entanglement that was created by the unitary collision operator in the second step.

Fourth, and last step of the QLG algorithm, we shift the f_i obtained in the previous step to its nearest neighbor. This step requires only classical communication between neighboring sites. The time is incremented after this step. Then, we loop back to step 1 and update the field of occupation probabilities over the lattice sites. In this way, we can continue to iterate forward in time and make a time-history record of the occupation probabilities, which in turn gives us the temporal evolution of the number density field.

4.1.2 First Implementation using NMR

In the first implementation of the Burgers equation, we chose the "Euler" angles in Eq. 4.4 to be $\phi = \zeta = \xi = 0$, and $\theta = \frac{\pi}{4}$. As a result, the general collision operator reduces to the quantum gate

$$\hat{C} = \begin{pmatrix} 1 & 0 & 0 & 0 \\ 0 & \frac{1}{\sqrt{2}} & \frac{1}{\sqrt{2}} & 0 \\ 0 & -\frac{1}{\sqrt{2}} & \frac{1}{\sqrt{2}} & 0 \\ 0 & 0 & 0 & 1 \end{pmatrix}, \tag{4.6}$$

and the equilibrium occupation probabilities for the Burgers equation are expressed:

$$f_i^{eq} = \frac{\rho}{2} + \frac{e_i}{\sqrt{2}}\left[1 - \sqrt{1 - \rho\left(1 - \frac{\rho}{2}\right)}\right], \tag{4.7}$$

where e_i is ± 1 for different qubits. Then we have the Burgers equation in standard form

$$\frac{\partial u}{\partial t} - u\frac{\partial u}{\partial x} = \nu\frac{\partial^2 u}{\partial x^2} \tag{4.8}$$

where $\nu = \frac{\Delta z^2}{2\Delta t}$ is the transport coefficient (viscosity term) and the flow field is defined as $u = c(\rho - 1)$.

A room-temperature solution of isotropically-labeled chloroform ($^{13}CHCl_3$) has been chosen for implementing the Burgers experiments. The hydrogen and the labeled carbon nucleus are served as qubits 1 and 2, and the difference of the gyro-magnetic ratio of two spins generates widely spaced resonant frequencies that allows us to address each spin independently.

The initial magnetization is specified by using a RF pulse shaped by the Fourier transform of the desired magnetization (transform of the initial number density profile). While applying the shaped pulse, a carbon decoupling sequence is performed to prevent the scalar coupling from interfering with the low power shaped pulses. In addition, the $\frac{\pi}{2}$ pulse, which rotates the information from the x-axis to the z-axis, is applied separately just after each initialization. This is done to keep the valuable information along the longitudinal direction where it will not be affected by the gradient and chemical shift. The encoding of initial states on both spins is accomplished in two steps: The initial carbon magnetization is recorded on the protons before being transferred to the carbons and followed by the initialization of proton magnetization. Furthermore, a short pulse sequence, called the *clean sequence*, is executed after the first swap gate to erase the phase distortion that may be caused by the decoupling sequence.

The unitary operator $\hat{C}$ can be decomposed of a sequence of RF pulses and scalar coupling. The product operators in the exponent commute with each other, resulting in $\hat{C} = \exp\left[-i\frac{\pi}{8}\sigma_x^H\sigma_y^C\right]\exp\left[i\frac{\pi}{8}\sigma_y^H\sigma_x^C\right]$ [2]. Both terms can be expanded as natural scalar

[2]The collision operator is achieved by the pulse sequence: $\left[\frac{\pi}{2}\right]_{-x}^{H,C} \rightarrow \frac{1}{2J} \rightarrow \left[\frac{\pi}{2}\right]_{x}^{H,C} \rightarrow \left[\frac{\pi}{2}\right]_{-y}^{H,C} \rightarrow \left[\frac{\pi}{4}\right]_{x}^{H}\left[\frac{\pi}{4}\right]_{-x}^{C} \rightarrow \frac{1}{2J} \rightarrow \left[\frac{\pi}{2}\right]_{y}^{H,C}$.

Hamiltonian couplings sandwiched with the appropriate single rotations, resulting in

$$\begin{aligned}\hat{C} &= \exp\left[-i\frac{\pi}{4}(\sigma_y^H+\sigma_y^C)\right]\exp\left[-i\frac{\pi}{4}\sigma_z^H\sigma_z^C\right]\exp\left[-i\frac{\pi}{8}(\sigma_x^H-\sigma_x^C)\right] \\ &\exp\left[i\frac{\pi}{4}(\sigma_y^H+\sigma_y^C)\right]\exp\left[-i\frac{\pi}{4}(\sigma_x^H+\sigma_x^C)\right]\exp\left[-i\frac{\pi}{4}\sigma_z^H\sigma_z^C\right]\exp\left[i\frac{\pi}{4}(\sigma_x^H+\sigma_x^C)\right].\end{aligned} \tag{4.9}$$

The exponential terms of single spin rotations are implemented by $\pi/2$ and $\pi/4$ pulses. The exponents of terms with $\sigma_z^H\sigma_z^C$ represent the natural internal Hamiltonian evolutions with time period $1/2J$.

The occupation numbers of each spin are obtained following the collision step by measuring the z-magnetization according to the following equation

$$f_i(z,t) = \frac{1}{2}\left[1+\langle\psi(z,t)|\sigma_z^i|\psi(z,t)\rangle\right]. \tag{4.10}$$

Since only σ_x and σ_y are observable in our NMR spectrometer, a $\pi/2$ pulse has been used to bring the z-magnetization into the transverse plane. The measurements are done in two separate experiments, where a SWAP gate is applied to bring the magnetization from carbon channel to the proton channel. This SWAP operation is done because the higher signal-to-noise ratio in the proton channel allows us to improve the accuracy of our implementation. During the "readout" process (Step 3), a week magnetic field gradient is applied to distinguish different sites. The observed proton signals are digitized and Fourier transformed, allowing us to record the spatially-dependent spin magnetization profile. The four main sections of the NMR implementation of QLG algorithm are graphically depicted in Figure 4-1.

The experiments have been performed on a lattice of 16 cells for 15 time steps, shown in Fig. 4-2. After ten iterations, the deviation between the experimental data and simulation results becomes significant. This indicates that our numerical simulations do not include all the potential error sources. However, some of them are small enough to be ignored for now. As described before, the "Euler" angles of the collision matrix are tunable and determines the viscosity term in the Burgers equation. We aims to choose another collision matrix for the Burgers equation, which contains a

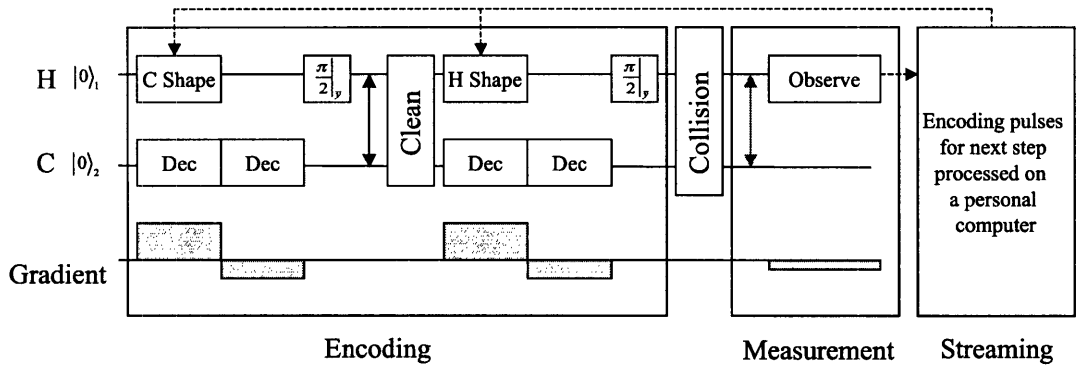

Figure 4-1: **QLG algorithm for the Burgers equation implemented in four steps.** Three horizontal lines represent proton spin, carbon spin and field gradients. Both starting magnetizations are encoded in proton channel first due to the high signal to noise ratio while decoupled in carbon channel to prevent interfering of scalar coupling. The collision operator is applied after the initialization. Measurement are also taken in two steps in the proton channel followed by data processing in a personal computer.

higher viscosity parameter, thus it takes less time steps to form the sharp front.

4.1.3 The Collision Matrix with Higher Viscosity Term

This time, ϕ, ζ, and ξ are still set to be zero, but $\cos\theta$ is selected to be 0.8 for convenience. In this particular case, the equilibrium occupation probabilities for the Burgers equation are determined by

$$f_i^{eq} = \frac{\rho}{2} + e_i \frac{5}{8}\left[1 - \sqrt{1 - \left(\frac{32\rho}{25}\right)\left(1 - \frac{\rho}{2}\right)}\right]. \tag{4.11}$$

The collision quantum operator [3] is written to be $\hat{C} = \exp\left[-i\frac{\pi}{4.882}\left(\sigma_x^H\sigma_y^C - \sigma_y^H\sigma_x^C\right)\right]$.

[3]The corresponding pulse sequence is the following: $\left[\frac{\pi}{2}\right]_{-x}^{H,C} \rightarrow \frac{1}{2J} \rightarrow \left[\frac{\pi}{2}\right]_{x}^{H,C} \rightarrow \left[\frac{\pi}{2}\right]_{-y}^{H,C} \rightarrow \left[\frac{\pi}{2.441}\right]_{x}^{H}\left[\frac{\pi}{2.441}\right]_{-x}^{C} \rightarrow \frac{1}{2J} \rightarrow \left[\frac{\pi}{2}\right]_{y}^{H,C}$.

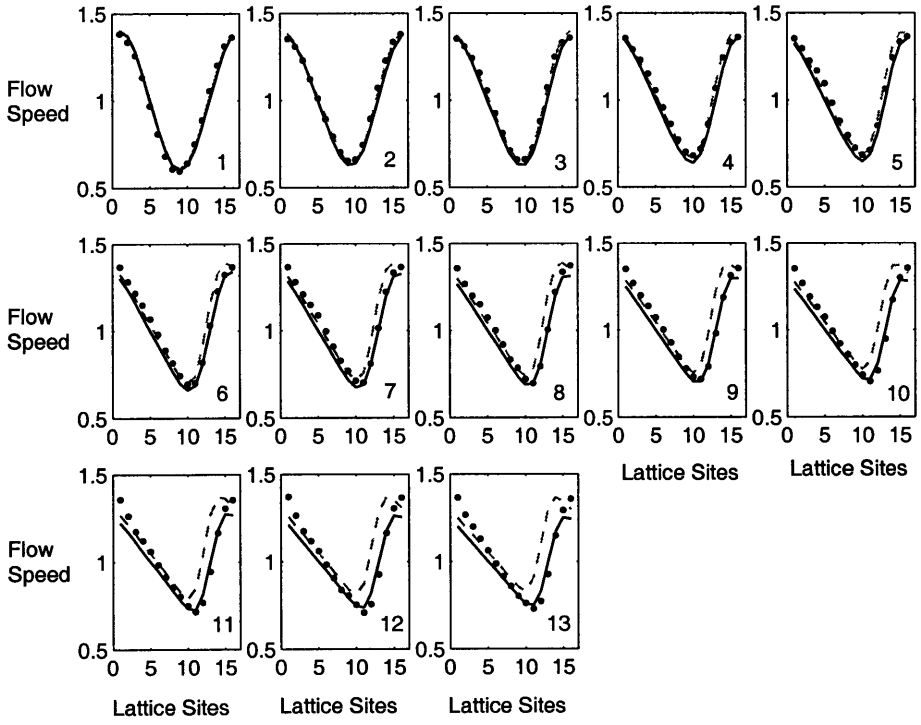

Figure 4-2: **Experiment results comparing with simulation and analytical solutions.** The experimental data (dots) are plotted together with the simulations (grey dash lines) and the analytical solutions (black solid lines) for 15 time steps on a lattice of 16 cells. The horizontal axis for each plot indicates the number of the lattice cells and vertical axis is the flow velocity. The numbers associated with each plot are the time steps. The deviation between the simulation and analytical solutions is mainly due to the accumulative errors in the collision operator. We also observed the deviation between the experimental data and simulation results, possibly introduced by inhomogeneity, self-diffusion.

The corresponding matrix representation is written as

$$\hat{C} = \begin{pmatrix} 1 & 0 & 0 & 0 \\ 0 & 0.8 & 0.6 & 0 \\ 0 & -0.6 & 0.8 & 0 \\ 0 & 0 & 0 & 1 \end{pmatrix}. \tag{4.12}$$

The viscosity term associated with this unitary operator is $\frac{1}{4}\frac{\Delta z^2}{\Delta t}$, which doubles the value in the previous one.

Nine successive time steps of the quantum algorithm have been implemented on 16 two-qubit sites, decipted in Fig. 4-3. Using the new collision matrix, the deviation between experimental data and simulation results has been reduced as we expected. Here, we have demonstrated shock-formation driven by a tunable viscosity parameter to show that the width of the shock front is not determined by implementation imperfections.

4.1.4 Numerical Simulations

The NMR numerical simulation has provided an alternative way to study the spectroscopic implementations. We have observed the deviation between the experimental data and analytical solutions due to the errors in the implementation. To explore the source and relative size of these errors, we simulated perfect experiments, each time adding controlled errors in four sections of the implementation:

- The linear approximation in the initialization
- Inefficiency of the decoupling sequence
- Swap gate errors
- Collision operator errors

The errors originating from the imperfect decoupling sequence caused least impact to the mass density, followed by the errors in the SWAP gates. The Fourier transform approximation executes a correct writing of the desired magnetization only to first

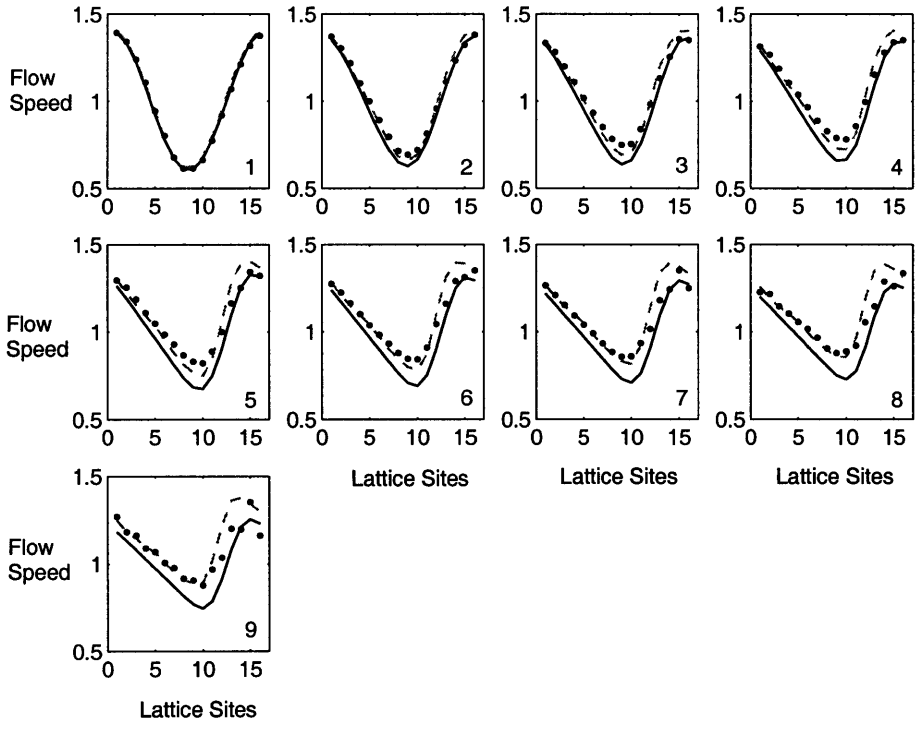

Figure 4-3: **Experimental data** The experimental data (dots) are plotted, together with plots of the analytical solutions (solid lines) and the numerical simulations (dash lines) of the NMR experiment. Nine time steps (numbers) of the algorithm have been carried out on 16 two-qubit sites. The vertical axis is associated with flow speed and the horizontal axis presents the lattice sites. The simulations closely match the data, suggesting that the deviation between the analytical results and the data can be attributed to four imperfection controls, discussed below, in the implementations.

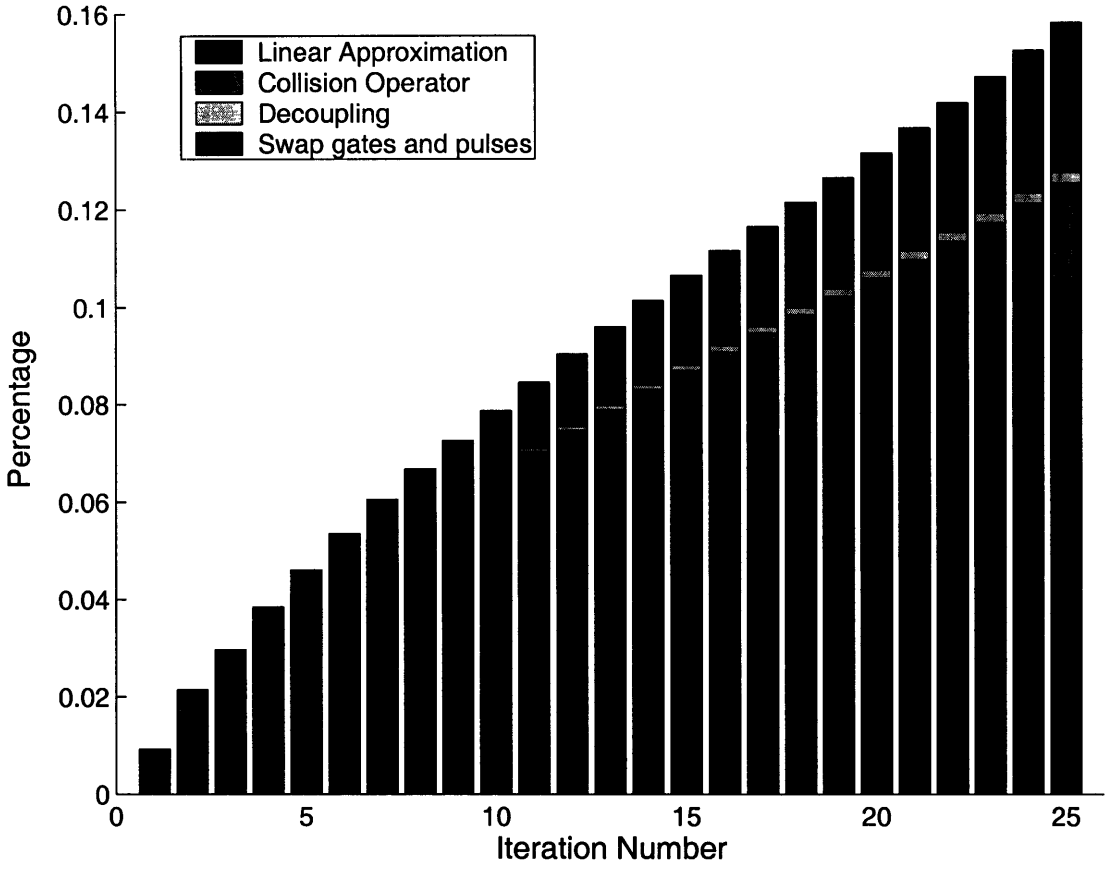

Figure 4-4: **Relative strength of four types of errors** We present the relative strength of each source here. Horizontal axis is denoted by time steps and vertical axis shows the difference between the simulation results with the analytical solutions. We notice that the deviation is mainly caused by the linear approximation at the beginning and the accumulated errors in the collision operators take over after a few time steps.

order in the overall flip angle. The largest deviations originated from realistic simulations of the collision gate. It is important to note that the simulated gate fidelities for the swap and collision gates, although imperfect, are still about 0.995. This suggests that the observed deviations are caused by the coherent buildup of errors through a few iterations, and not just by the individual errors from a single gate. The complete simulation result, showing the relative size of each error, is plotted in Fig. 4-4.

In the NMR implementations to date there are two important sources of systematic errors: (1) a linear approximation relating the excited magnetization to the

Fourier components of the shaped RF pulse; and (2) errors from the repeated collision operators. Here we explore the impact of these errors on a simple computation and illustrate a simple means of reducing the accumulated errors. In summary, one of the most important challenges to implement a useful type-II quantum architecture is to avoid the accumulation of systematic errors. In the next section, our discussion aims to an alternative method to mitigate the growth of systematic errors.

4.1.5 The Collision Operator with Modulated Phases

The first-order accurate Fourier approximation was expected to be the dominant error source in the NMR implementation. However, NMR simulations with controlled errors shows that the systematic error induced by the experimental implementation of the unitary collision operator associated with the QLG algorithm is the major challenge. Replacing the single collision operator with a set of operators to randomize errors allows us to improve the robustness of the implementation.

In the implementation of the Burgers equation, we also observed deviations between the numerically predicted data points and analytically predicted solutions. The major error sources in the NMR implementation are known, so to explore the source and relative strength of these errors, we have simulated the NMR experiments. The major error source in this implementation is the collision operator, and it is introduced by ignoring the scalar coupling between proton and carbon during the RF pulses. When applying a RF pulse on the proton qubit, the Hamiltonian in the rotating form is $H = 2\pi J\sigma_z^H\sigma_z^C + \gamma_H B_1\sigma_x^H$, where B_1 is the strength of the RF pulse. With the presence of the scalar coupling, a small portion of the proton magnetization has been transfered to the carbon qubit. Therefore, the applied propagator can be recast as $U = U_{\text{desired}}U_{\text{error}}$.

The error in the collision operator is a systematic error that builds up throughout the successive time steps. Although this is not the significant error at the beginning of the implementation, it eventually dominates the first-order error due to the Fourier approximation and becomes the dominant issue after just several time step interactions. Notice that while the reduction of the initial magnetization from the Fourier

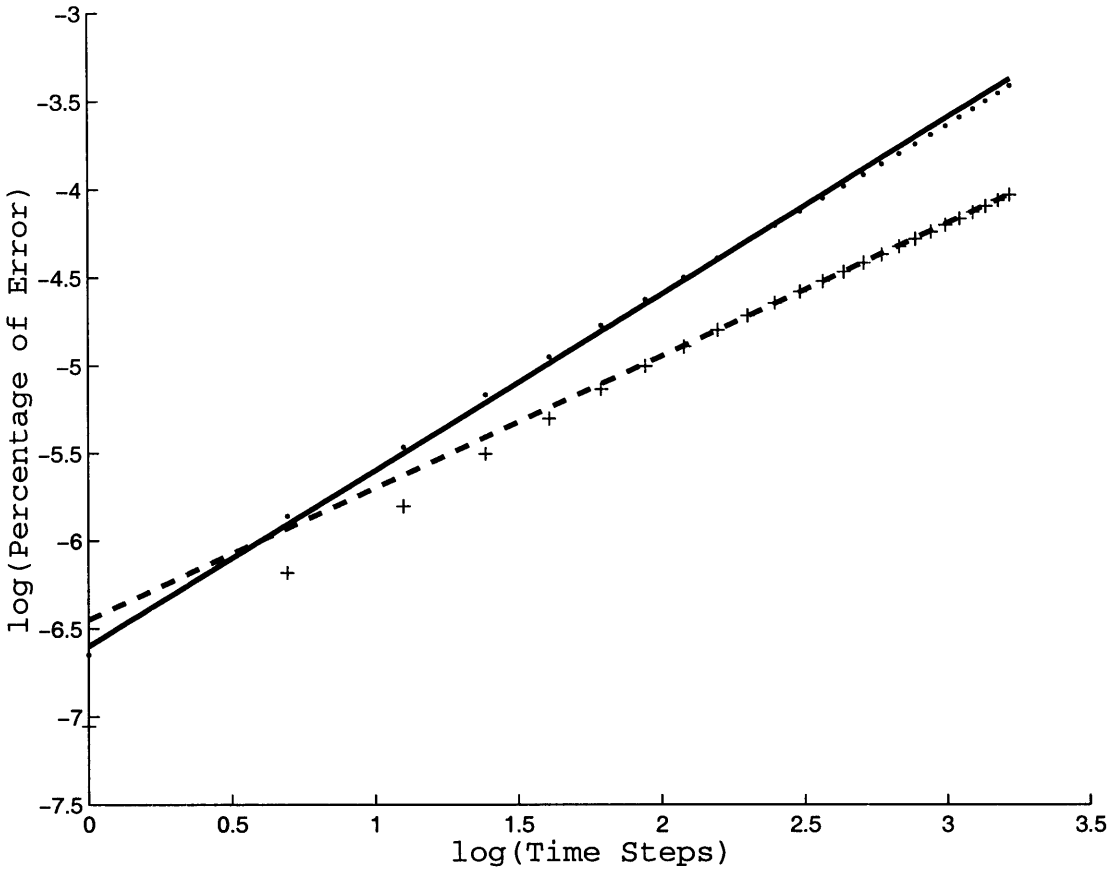

Figure 4-5: **Systematic errors** The growth of the systematic errors due to the collision operator in two NMR implementation. The single collision operator data (dots) is fit (solid line) with a line of slope 1, which shows linear growth of the error. The collision operator data with modulated phases (pluses) is the fit with a line of slope 3/4 (dashed line). The buildup of the systematic errors has been slowed down by proposed method. However, the systematic errors have not been totally converted into random errors.

transform is systematic, since the magnetization profile is changing the errors are not precisely repeated. In the collision operator, however, the errors are exactly the same from step to step. In addition we expect that the radio frequency inhomogeneity leads to strongly correlated errors in the lattice encoding. Hence, we have proposed replacing a single collision operator with a set of collision operators that have similar fidelity but randomized error terms.

Since the collision operator for the Burgers equation is a zero-order coherence term, the collision operator commutes with the rotation operator. Therefore, we

apply a 90° rotation operator to the collision operator at each step to mitigate error growth. Consequently, a dramatic improvement is observed as shown in Fig. 4-5. On a logarithmic plot, the simulation results fit a line with a slope of 3/4. If the error terms in the collision operators were totally randomized and hence followed a Gaussian distribution, the best-fit regression line should have had a slope of 1/2. The deviation between our simulation data and the ideal Gaussian case indicates residual systematic error in the collision operator. In a future study, we may use strongly modulated pulses to randomize the error terms [31].

The experimental number densities are over-plotted in Fig. 4-6 with the exact analytical solutions. Eight successive time steps of the quantum algorithm were implemented on 16 two-qubit sites. An improvement of our present experimental approach using collision operators with modulated phases is observed. The agreement of the data to the analytical solutions is encouraging and suggests that totally randomizing error terms in the collision operator may offer further improvement.

4.2 Conclusion

From the simulation, we find the major error sources are due to imperfect control of the quantum spin system and the Fourier approximation associated with setting its magnetization profile. Our proposed method for converting the systematic errors into random errors is effective. The improvement we achieve relative to the previous experiment is encouraging, and it demonstrates the possibility of using the same technique in future studies. The closeness of the numerical data to the exact analytical results for the nonlinear Burgers equation further proves the practicality of implementing the QLG algorithm using a spatial NMR technique. In addition, although the limitation of the Fourier approximation is not dominant, the problem of precisely initializing a lattice of QIPs still remains an open issue.

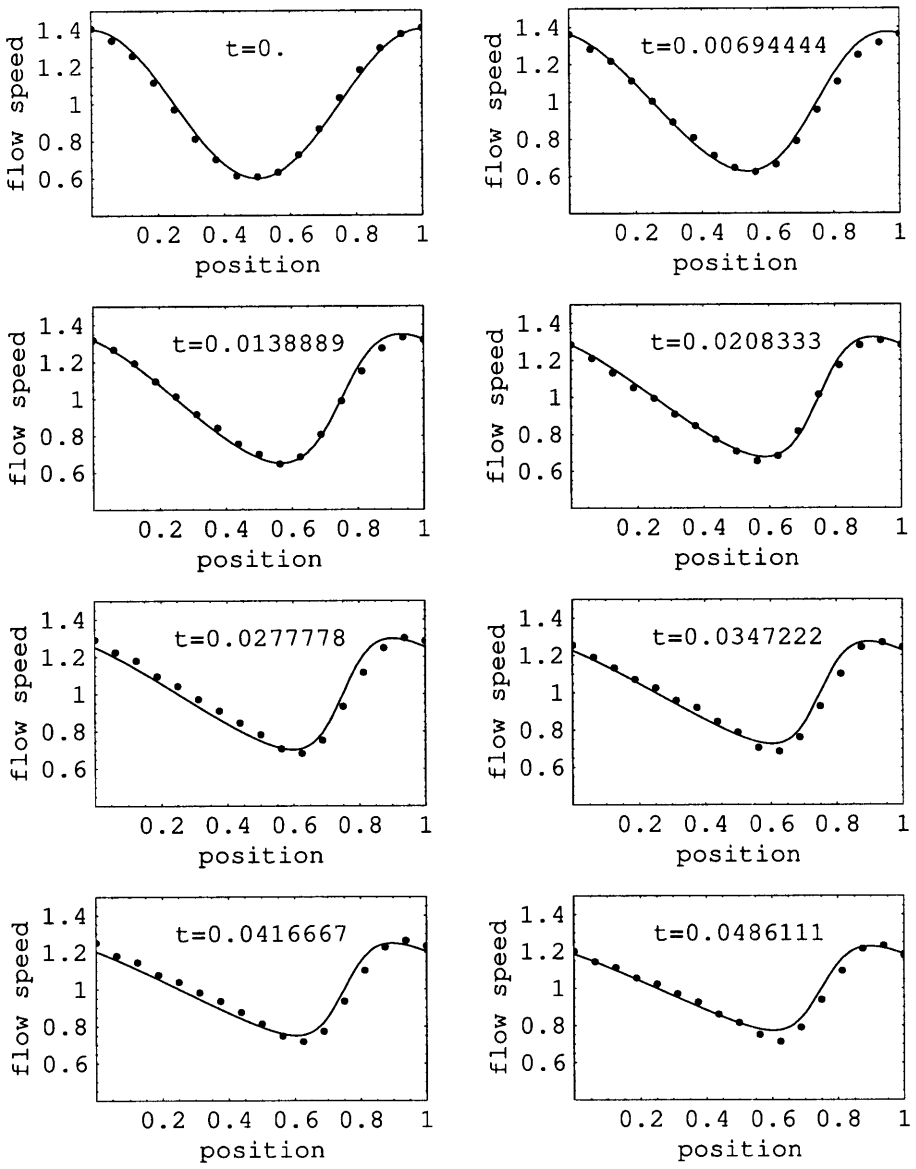

Figure 4-6: **Experiment data versus analytical results** The experimental data are plotted together with the analytical solutions for 8 time steps on a lattice of 16 parallel two-qubit QIPs. Viscosity: $\frac{1}{4}\frac{\Delta x^2}{\Delta t}$. Experimental NMR data (dots) versus analytical solution (curves). Randomizing the error terms in the collision operator has improved the experimental results dramatically.

4.3 Other Error Sources

Other potential sources of errors include signal to noise, the state fidelity of the starting pseudo pure state, and gradient switching time. In addition, the random self-diffusion of the liquid molecules in the presence of a strong gradient can result in a substantial loss of signal. Although these errors were not significant in our implementation, they are likely to become important as more complicated algorithms are executed on larger lattices.

In particular, molecular diffusion over the time of an operation places a lower bound on the physical size of the volume element corresponding to each site in the computation. In the 1-D case discussed here, the root-mean-squared displacement ($\Delta z = \sqrt{2Dt}$) for chloroform ($D = 2.35 \times 10^{-5} cm^2/s$) is about $10.8 \mu m$ over the $25ms$ needed for encoding and the collision operator. Since the actual volume element were about $625 \mu m$ across, this resulted in a negligible mixing of the information in adjacent sites. However, it is clear that for this approach to type-II quantum computer to remain viable for large matrixes and more complex collision operators the physical size of the sample must grow with the size of the problem.

4.4 Discussion

It has been suggested by Peter Love in [32] that the transition matrix $\mathbf{A}$ in the type-II lattice gas algorithms for the Burgers equation may not be a doubly stochastic matrix. It should be clear here that the transition matrix defining the lattice Boltzmann equation is not the collision operator defined in the algorithms. We begin the discussion by deriving the transition matrix $\mathbf{A}$ from the unitary collision operator $\hat{C}$. The occupation numbers in the classical Boltzmann model are encoded as the diagonal terms in the density matrix $\mathbf{n} = [(1-f_1)(1-f_2), (1-f_2)f_1, f_2(1-f_1), f_1 f_2]$. The collision step of the Boltzmann model is given by the multiplication of the vector $\mathbf{n}$ by the transition matrix that satisfies normalization and semi-detailed balance. In our type-II simulation, the result of the collision step is reproduced by conjugating

the density matrix by the collision operator. The transition matrix is denoted by the effect of this conjugation on the diagonal elements in the density matrix.

As mentioned earlier in this chapter, the collision transformation can be expressed by a general block-diagonal unitary matrix with complex coefficient:

$$\hat{C} = \begin{pmatrix} 1 & 0 & 0 & 0 \\ 0 & e^{i\phi}e^{i\xi}\cos\theta & e^{i\phi}e^{i\zeta}\sin\theta & 0 \\ 0 & -e^{i\phi}e^{-i\zeta}\sin\theta & e^{i\phi}e^{-i\xi}\cos\theta & 0 \\ 0 & 0 & 0 & 1 \end{pmatrix}. \tag{4.13}$$

Therefore, quantum transition map on the diagonal elements in the density matrix can be written as:

$$\begin{aligned} \rho'_{11} &= \rho_{11} \\ \rho'_{22} &= \cos^2\theta\rho_{22} + \sin^2\theta\rho_{33} + e^{-i(\xi-\zeta)}\cos\theta\sin\theta\rho_{32} + e^{i(\xi-\zeta)}\cos\theta\sin\theta\rho_{23} \\ \rho'_{33} &= \sin^2\theta\rho_{22} + \cos^2\theta\rho_{33} - e^{-i(\xi-\zeta)}\cos\theta\sin\theta\rho_{32} - e^{i(\xi-\zeta)}\cos\theta\sin\theta\rho_{23} \\ \rho'_{44} &= \rho_{44} \end{aligned} \tag{4.14}$$

The transition matrix then contains two components: classical diffusive part and quantum mechanical part as described:

$$\mathbf{A} = \begin{pmatrix} 1 & 0 & 0 & 0 \\ 0 & \cos^2\theta & \sin^2\theta & 0 \\ 0 & \sin^2\theta & \cos^2\theta & 0 \\ 0 & 0 & 0 & 1 \end{pmatrix} + \frac{1}{2}\cos 2\theta \begin{pmatrix} 0 & 0 & 0 & 0 \\ 0 & e^{-i(\xi-\zeta)}\frac{\rho_{32}}{\rho_{22}} & e^{i(\xi-\zeta)}\frac{\rho_{23}}{\rho_{33}} & 0 \\ 0 & -e^{-i(\xi-\zeta)}\frac{\rho_{32}}{\rho_{22}} & -e^{i(\xi-\zeta)}\frac{\rho_{23}}{\rho_{33}} & 0 \\ 0 & 0 & 0 & 0 \end{pmatrix}, \tag{4.15}$$

where the quantum mechanical part gives rise non-diffusive behavior, the nonlinear shock formation characteristic of the Burgers equation. Furthermore, the quantum mechanical part brings the off-diagonal information to the diagonal elements, introducing local quantum superposition and entanglement. Thus, the new values of the occupation probabilities in the lattice Boltzmann model is not, exclusively, determined by the occupation numbers in the previous step.

The unitarity of $\hat{C}$ implies that the classical part of the transition matrix $\mathbf{A}$ obeys normalization and semi-detailed balance. It is trivia to realize that the sum of each column in the second term is zero. Thus, any arbitrary collision operator for the Burgers equation obeys the semi-detailed balance. To formulate a sufficient normalization constraint, we simplify the constraint to be

$$e^{-i(\xi-\zeta)}\frac{\rho_{32}}{\rho_{22}} + e^{i(\xi-\zeta)}\frac{\rho_{23}}{\rho_{33}} = 0. \tag{4.16}$$

Only when Eq. 4.16 is satisfied, the collision transformation is a doubly stochastic matrix. Therefore, it leaves us an open issue about the algorithms and further discussion should be invoked.

The systematic error that we discussed in this chapter is not caused by this open problem, but introduced by the imperfect implementations. Details about the quantum control of the NMR system are accessible in [36, 37, 38, 39].

Chapter 5

Linear Approximation

We utilize the magnetic image technique to slice NMR spin ensemble into a lattice of cells and address all the spatial locations simultaneously. This technique is essentially the application of shaped RF pulses in the presence of a gradient field as a means of exciting selective frequencies. If the flip angle of the shaped pulse is small and the excited magnetizations, to a good approximation, are proportional to the Fourier transform of the RF waveform. As a result, the RF waveform can also be determined by the inverse Fourier transform of the desired transverse magnetization. The above technique allows the encoding of arbitrary shapes at the various spatial locations in our experiment. However, this Fourier approach for determining the frequency selectivity of a pulse sequence is only accurate to the first order and generates potential error sources.

We aims to remove the linear approximation by mapping lattice cells to a set of Fourier components in the k-space, a space reciprocal to the spatial locations. This new approach gives us the freedom to perform the streaming step quantum mechanically by controlling the linear magnetic field gradients. It may arise new applications using this particular architecture for quantum lattice gas algorithms.

We have chosen to the diffusion equation to explore the NMR implementation using the k-space mapping. Diffusion equation provides a neat and robust test since low frequencies Fourier components in the magnetization profile are less sensitive to errors.

5.1 Mapping to k-space

In a type-II quantum lattice gas algorithm, the occupation probabilities are encoded to the wave function of lattice sites. Each occupation probability $f_i(z,t)$ is represented as the quantum mechanical expectation value of finding a two-level system in its excited state. The combined two-qubit wave function for a single node becomes $|\psi(z,t)\rangle = \sqrt{f_1 f_2}|11\rangle + \sqrt{f_1(1-f_2)}|10\rangle + \sqrt{(1-f_1)f_2}|01\rangle + \sqrt{(1-f_1)(1-f_2)}|00\rangle$. The collision operator is a unitary evolution matrix applied homogeneously across all the lattice sites causing local quantum superposition and entanglement, $|\psi'(z,t)\rangle = \hat{C}|\psi(z,t)\rangle$. Measurement process is a non-unitary action that destroys all the superpositions and entanglements caused by the previous step, resulting in $f_i(z,t) = \langle\psi(z,t+\Delta t)|\hat{n}_i|\psi(z,t+\Delta t)\rangle$, where $\hat{n}_i$ are the number operators. In practice, the occupation numbers must be determined by repeated measurement of a single realization or by a single measurement over a statistical ensemble. The NMR ensemble nature make this measurement particular simple.

The wave function method outlined above is adequate for simple problems that consists of few spins, but becomes tedious to describe more complicated cases involving more spins. The magnetic state of the NMR ensemble, therefore, is conveniently defined using the density matrix formalism. The density matrix corresponded to the wave functions is

$$\rho(z,t) = |\psi(z,t)\rangle\langle\psi(z,t)|. \tag{5.1}$$

and the collision step can be reformulated as

$$\rho'(z,t) = \hat{C}\rho(z,t)\hat{C}^{\dagger}. \tag{5.2}$$

The measurement process consists in taking the trace of the measurement operator acting on the density matrix of the system being measured:

$$< n_i >= tr\left[\rho(z,t)\hat{n}_i\right]. \tag{5.3}$$

A similar presentation of the lattice can be formulated in the k-space by creating

the correspondence between a lattice node with a Fourier component, generated by magnetic field gradients. Once a static field gradient is applied, the spin procession frequency varies linearly with the position along the z direction. It induces the transverse phase to accumulate linearly with position as well. The gradient field, therefore, modulate the transverse magnetization into a spatial helix, referred as a Fourier component characterized with it wave number k. A RF pulse can modulate the phase and amplitude of each Fourier helix and also produce amplitude modulated magnetization gratings along z direction by transforming the transverse magnetizations to longitudinal direction. However, a RF pulse does not change the pitch of the grating and only the gradients can change the k value of each component to another in the k-space. Due to the linear nature of the k-space, each separate Fourier component may be treated independently. The corresponding formalism of the density matrix 5.1 results in

$$\rho(k,t) = |\psi(k,t)\rangle\langle\psi(k,t)|, \tag{5.4}$$

where k indicates a lattice cell. The evolution of the collision step is described by the following equation

$$\rho'(k,t) = \hat{C}\rho(k,t)\hat{C}^{\dagger}. \tag{5.5}$$

Then, the measurement is given by

$$< \hat{n_i} >= tr\left[\rho(k,t)\hat{n_i}\right]. \tag{5.6}$$

5.2 NMR Implementation

The same room-temperature solution of labeled chloroform used in the previous experiments has been selected. The resonant frequencies of the two spins, hydrogen and labeled carbon, in this heteronuclear molecule is about 225MHz apart in 10 T magnet. Therefore, a single pulse on resonance with one spin will not affect the other. The interaction term between the spins can be characterized by the scalar coupling constant $J = 214Hz$. More details about the sample can be found in Chapter 3.

5.2.1 Encoding

Individual addressing the sites of the lattice is established by a sequence of RF pulses followed by the gradient Hamiltonians. We begin by studying the evolution of a one-spin system and the small angle approximation is invoked here to simplify the calculation. Then the discussion moves to a weakly coupled two-spin system. In this system, there are two important challenges to implement a type-II quantum architecture: (1) lattice initialization to an identical Fourier component; and (2) the internal Hamiltonian interfering information between spins. We demonstrate that the usage of π pulses on one spin in conjunction with two static gradients for the same duration can give the desired results. Wisely selecting the gradient strengths, the Fourier helices associated with both spins can have same wave number even though they have different gyro-magnetic ratios. The π pulses modulate the interaction Hamiltonian and refocus scalar term after one period of the sequence: the system, thus, can be treated independently as two one-spin systems.

First, consider the Hamiltonian for a one-spin system subjected to a RF pulse applied in the y-direction followed by a linear field gradient in the z-direction. The RF Hamiltonian is

$$H_{RF} = -\frac{1}{2}\omega_y \sigma_y. \tag{5.7}$$

and the gradient Hamiltonian is

$$H_G = -\frac{1}{2}\left(\gamma \frac{\partial B_z}{\partial z} z\right)\sigma_z = -\frac{1}{2}\gamma G z \sigma_z, \tag{5.8}$$

where ω_y is a constant value during the pulse time τ and the gradient term is a linearly varying static field. The static gradient strength is denoted by G. The evolution of the period $\tau + \Delta t$ becomes

$$U(t = \tau + \Delta t) = \exp\left[\frac{i}{2}\Delta k_z z \sigma_z\right] \exp\left[\frac{i}{2}\omega_y \tau \sigma_y\right] \tag{5.9}$$

where Δk_z is the wavenumber, parametered as $\Delta k_z = \gamma \frac{\partial B_z}{\partial z}\Delta t$. The evolution of an

initial density matrix $\rho_0 = \sigma_z$ through a single period yields

$$\rho(\tau + \Delta t) = U\sigma_z U^\dagger = \sin(\omega_y \tau) \exp\left[\frac{i}{2}\Delta k_z z \sigma_z\right] \sigma_x \exp\left[-\frac{i}{2}\Delta k_z z \sigma_z\right] + \cos(\omega_y \tau)\sigma_z. \tag{5.10}$$

If the small angle approximation applies, the density matrix becomes

$$\rho(\tau + \Delta t) \approx \omega_y \tau \exp\left[\frac{i}{2}\Delta k_z z \sigma_z\right] \sigma_x \exp\left[-\frac{i}{2}\Delta k_z z \sigma_z\right] + \sigma_z. \tag{5.11}$$

Another period evolution will affect the σ_z term as described above, creating the new magnetization helix and incrementing wavenumber by Δk_z. The final result is the formation of many Δk_z components

$$\sigma_z \rightarrow \sum_{n=1}^{N} \omega_y(n)\tau \exp\left[\frac{i}{2} n \Delta k_z z \sigma_z\right] \sigma_x \exp\left[-\frac{i}{2} n \Delta k_z z \sigma_z\right] + \sigma_z. \tag{5.12}$$

Each term is summation can be interpreted as a cylindrical Fourier component of the transverse magnetization weighted by the RF nutation rate $\omega_y(n)$.

Next step, we will consider the evolution of two weakly coupled spins with gyromagnetic ratio γ_H and γ_C,respectively. The RF Hamiltonian is expressed as the sum of two single RF terms because of the realization that both spins are addressed independently through two channels.

$$H_{RF} = -\frac{1}{2}\omega_y^1 \sigma_y^1 - \frac{1}{2}\omega_y^2 \sigma_y^2 \tag{5.13}$$

and the gradient Hamiltonian gives

$$H_G = -\frac{1}{2}(\gamma_H + \gamma_C)\frac{\partial B_z}{\partial z} z\sigma_z = -\frac{1}{2}(\gamma_H + \gamma_C) G z \sigma_z, \tag{5.14}$$

Consequently, the evolution operator of a single period consists of two exponential terms: a single spin rotation and gradient evolution term. Since the internal Hamiltonian commute with the gradient Hamiltonian, the gradient evolution can be expressed

by two separate terms as well,

$$\begin{aligned} U(t=\tau+\Delta t) &= \exp\left[\frac{i}{2}(\Delta k_z^1\sigma_z^1+\Delta k_z^2\sigma_z^2)z+\frac{i\pi J}{2}\sigma_z^1\sigma_z^2\Delta t\right]\exp\left[\frac{i}{2}(\omega_y^1\sigma_y^1+\omega_y^2\sigma_y^2)\tau\right] \\ &= \exp\left[\frac{i}{2}(\Delta k_z^1\sigma_z^1+\Delta k_z^2\sigma_z^2)z\right]\exp\left[\frac{i\pi J}{2}\sigma_z^1\sigma_z^2\Delta t\right] \\ &\quad \exp\left[\frac{i}{2}(\omega_y^1\sigma_y^1+\omega_y^2\sigma_y^2)\tau\right], \end{aligned} \tag{5.15}$$

where the exponential terms of $\sigma_z^1\sigma_z^2$ are attributed to the internal Hamiltonian. One may realize that the scalar coupling evolution has not been considered during the RF pulse. It has been neglected because the total nutation frequencies induced by the RF Hamiltonians are much stronger then the interaction constant.

An initial density matrix $\sigma_z^1+\sigma_z^2$ through a single period becomes

$$\begin{aligned} \rho = U(\sigma_z^1+\sigma_z^2)U^\dagger &= \sigma_z^1+\sigma_z^2+\exp\left[\frac{i}{2}(\Delta k_z^1\sigma_z^1+\Delta k_z^2\sigma_z^2)z\right] \\ &\quad \exp\left[\frac{i\pi J}{2}\sigma_z^1\sigma_z^2\Delta t\right](\omega_y^1\tau\sigma_x^1+\omega_y^2\tau\sigma_x^2)\exp\left[\frac{-i\pi J}{2}\sigma_z^1\sigma_z^2\Delta t\right] \\ &\quad \exp\left[\frac{-i}{2}(\Delta k_z^1\sigma_z^1+\Delta k_z^2\sigma_z^2)z\right]. \end{aligned} \tag{5.16}$$

A string of π pulses on the first spin is applied to modulate the Fourier components, remove the chemical shift, and refocus the scalar interactions. The π pulse along x modulates σ_z, σ_y terms with minus signs and leaves σ_x operator unchanged: $\sigma_x \rightarrow \sigma_x, \sigma_y \rightarrow -\sigma_y, \sigma_z \rightarrow -\sigma_z$. After a single π pulse along x on qubit 1, the density matrix picks up a minus sign for all the terms which contain σ_z^1 and σ_y^1:

$$\begin{aligned} \rho &= -\sigma_z^1+\sigma_z^2+\exp\left[\frac{-i}{2}(-\Delta k_z^1\sigma_z^1+\Delta k_z^2\sigma_z^2)z\right]\exp\left[\frac{-i\pi J}{2}\sigma_z^1\sigma_z^2\Delta t\right] \\ &\quad (\omega_y^1\tau\sigma_x^1+\omega_y^2\tau\sigma_x^2)\exp\left[\frac{i\pi J}{2}\sigma_z^1\sigma_z^2\Delta t\right]\exp\left[\frac{i}{2}(-\Delta k_z^1\sigma_z^1+\Delta k_z^2\sigma_z^2)z\right]. \end{aligned} \tag{5.17}$$

The operator, given by the application of a static gradient for another period Δt with a variant strength, causes the internal Hamiltonian average over at the end of the

period,

$$\begin{aligned}\rho &= -\sigma_z^1 + \sigma_z^2 + \exp\left\{\frac{i}{2}\left[(\Delta k_z^{1\prime} - \Delta k_z^1)\sigma_z^1 + (\Delta k_z^{2\prime} + \Delta k_z^2)\sigma_z^2\right] z\right\} \\ &\quad (\omega_y^1 \tau \sigma_x^1 + \omega_y^2 \tau \sigma_x^2) \exp\left\{\frac{-i}{2}\left[(\Delta k_z^{1\prime} - \Delta k_z^1)\sigma_z^1 + (\Delta k_z^{2\prime} + \Delta k_z^2)\sigma_z^2\right] z\right\},\end{aligned} \tag{5.18}$$

where wave numbers of corresponding Fourier components on both spins are increased by $\Delta k_z^{1\prime}$ and $\Delta k_z^{2\prime}$ respectively. Another π pulse, following the magnetic gradient, is performed to reverse the minus signs on all the σ_z^1 terms,

$$\begin{aligned}\rho &= \sigma_z^1 + \sigma_z^2 + \exp\left\{\frac{i}{2}\left[(\Delta k_z^1 - \Delta k_z^{1\prime})\sigma_z^1 + (\Delta k_z^2 + \Delta k_z^{2\prime})\sigma_z^2\right] z\right\} \\ &\quad (\omega_y^1 \tau \sigma_x^1 + \omega_y^2 \tau \sigma_x^2) \exp\left\{\frac{-i}{2}\left[(\Delta k_z^1 - \Delta k_z^{1\prime})\sigma_z^1 + (\Delta k_z^2 + \Delta k_z^{2\prime})\sigma_z^2\right] z\right\}.\end{aligned} \tag{5.19}$$

We can rewrite Eq. 5.19 as Eq. 5.20 if the actions of the gradient Hamiltonians on both qubits are identical, $\Delta k_z^1 - \Delta k_z^{1\prime} = \Delta k_z^2 + \Delta k_z^{2\prime} = \Delta k_z$.

$$\rho = \sigma_z^1 + \sigma_z^2 + \exp\left[\frac{i}{2}\Delta k_z(\sigma_z^1 + \sigma_z^2)z\right](\omega_y^1 \tau \sigma_x^1 + \omega_y^2 \tau \sigma_x^2) \exp\left[\frac{-i}{2}\Delta k_z(\sigma_z^1 + \sigma_z^2)z\right]. \tag{5.20}$$

Effects of both field gradients accumulate on the carbon nucleus, while the second gradient attenuates, to some extent, the first one for the proton spin. Thus, the deviation between the k values caused by the different gyro magnetic ratios is compensated by applying the above pulse sequence. The condition is satisfied if the ratio of two gradients obeys

$$\frac{G_1}{G_2} = \frac{\gamma_H + \gamma_C}{\gamma_H - \gamma_C}. \tag{5.21}$$

The procedure described above is illustrated in Fig. 5-1.

After n periods application of the composition of RF pulses and gradients, it gives

$$\begin{aligned}&\sigma_z^1 + \sigma_z^2 \rightarrow \sigma_z^1 + \sigma_z^2 + \\ &\sum_{n=1}^{N} \exp\left[\frac{i}{2} n\Delta k_z(\sigma_z^1 + \sigma_z^2)z\right]\left[\omega_y^1(n)\tau\sigma_x^1 + \omega_y^2(n)\tau\sigma_x^2\right] \exp\left[\frac{-i}{2} n\Delta k_z(\sigma_z^1 + \sigma_z^2)z\right].\end{aligned} \tag{5.22}$$

The exact solution can be achieved and it is given in [30],

$$\sigma_z^1 + \sigma_z^2 \rightarrow \prod_{n=1}^{N} \cos(\omega_y^1(n)\tau)\sigma_z^1 + \prod_{n=1}^{N} \cos(\omega_y^2(n)\tau)\sigma_z^2 + \tag{5.23}$$
$$\sum_{n=1}^{N} \exp\left[\frac{i}{2} n\Delta k_z(\sigma_z^1 + \sigma_z^2)z\right]\left[A_N^1(n)\sigma_x^1 + A_{N,z}^1(n)\sigma_z^1 + A_N^2(n)\sigma_x^2 + A_{N,z}^2(n)\sigma_z^2\right]$$
$$\exp\left[\frac{-i}{2} n\Delta k_z(\sigma_z^1 + \sigma_z^2)z\right].$$

For a train of RF pulses of nutation angles $\omega_y^1(n)$ and $\omega_y^2(n)$ all with the same phase, the nth transverse and longitudinal Fourier series coefficient after Nth pulses, may be determined from the previous coefficients by the recursion relationships

$$\begin{aligned} A_N^i(n) &= A_{N-1}^i(n-1)\cos^2(\omega_y^i(n)\tau/2) - A_{N-1}^i(-n-1)\sin^2(\omega_y^i(n)\tau) \\ &\quad -A_{N-1,z}^i(|n|)\sin(\omega_y^i(n)\tau)\left(\frac{\epsilon_n}{2}\right) \\ A_{N,z}^i(n) &= \left[A_{N-1}^i(n-1) + A_{N-1}^i(-n-1)\right]\frac{\sin(\omega_y^i(n)\tau)}{\epsilon_n} \\ &\quad +A_{N-1,z}^i(n)\cos(\omega_y^i(n)\tau) \end{aligned} \tag{5.24}$$

where $\epsilon_n = 1 + \delta_n$. Initial conditions have to satisfy that $A_{0,z}^i(n) = \delta_n$ and that all $A_0^i(n) = 0$. The appropriate choice of the nutation angles enable us to construct arbitrary density matrix.

5.2.2 Collision

The choice of the particular components of the unitary collision operator determines the form of the macroscopic effective field theory and values of its transport coefficients. The same collision operator for the diffusion equation has been chosen:

$$\hat{C} = \exp\left[-i\frac{\pi}{8}\left(\sigma_x^1\sigma_x^2 + \sigma_y^1\sigma_y^2 + \sigma_z^1\sigma_z^2\right)\right]. \tag{5.25}$$

We already learn that a RF pulse does not shift the k value of each component, indicating the information between the neighbors cannot be manipulated using RF pulses and scalar evolution. Therefore, the local quantum collision gate can be accomplished

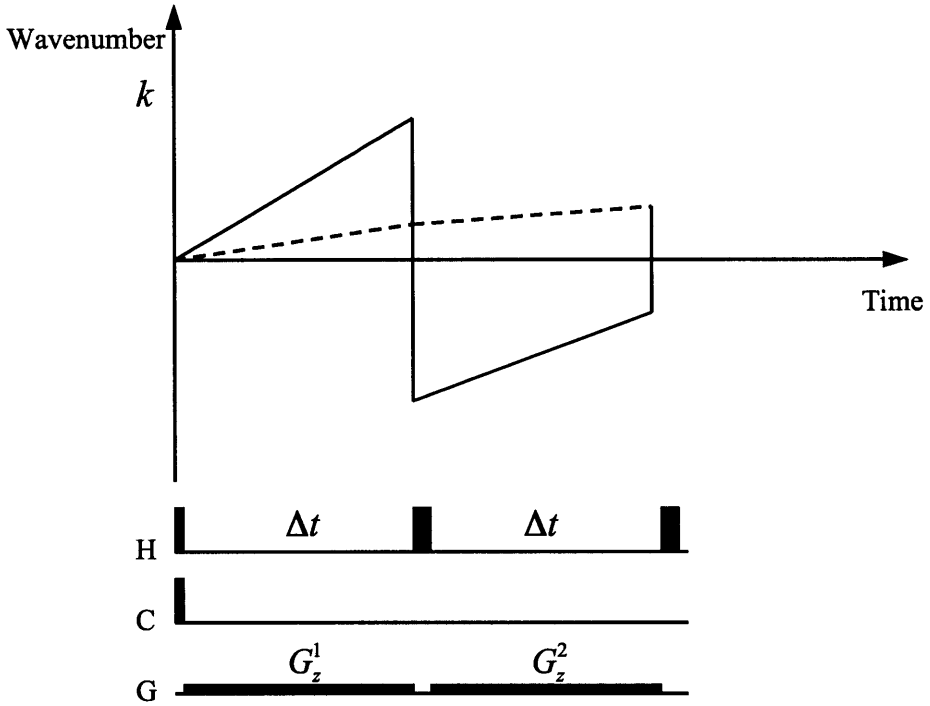

Figure 5-1: **One step in the initialization** One period of the sequence used in the initialization and corresponding changes of k values in the k-space are presented. The solid line, in the k space diagram, illustrates the shift of the wave number for the hydrogen spin while the time iterates forwards. The dash line gives the movement of k value for the carbon. At the end of the sequence, the wave numbers of the characteristic Fourier components of both spins are incremented by the same amount. Below the plot, the pulse sequence is demonstrated.

by the same pulse sequence described in Chapter 3.

5.2.3 Measurement

The occupation numbers resulting from the collision are obtained by measuring the z-magnetization, corresponding to $n_i = \frac{1}{2}(1 + \sigma_z^i)$. Since only the σ_x^i and σ_y^i operators are directly observable, a $\pi/2$ pulse transformed the z-magnetization into x-magnetization.

The measurements are carried out in two separate experiments, where a SWAP gate is applied to bring the magnetization from carbon channel to the proton channel due to the higher signal-to-noise ratio in the proton channel.

During the process, a weak magnetic field gradient is applied to refocus the gradient Hamiltonians. It is easy to realize that the signal is only observable while the k value is around zero. Otherwise, the ensemble signal is averaged over across the sample. Note that a spatial map of spin density in the sample weighted in some fashion during the measurement. The corresponding modulation function for our finite and uniform sample is a sinc function. Instead of observing a sharp magnetization peak, the signal is specified by a sinc function. Hence, the readout gradient has to be weak enough to separate the overlap between two sinc functions induced by the spin density.

5.2.4 Streaming

The last step of the QLG algorithm, we shift the occupation numbers obtained in the previous step to its nearest neighbors. In the k-space, the streaming step can be easily created by the application of linear field gradients sandwiched with π pulses: $G_3(z)\Delta t \rightarrow [\pi]_x^H \rightarrow G_4(z)\Delta t \rightarrow [\pi]_x^H$, where $G_3(z)$, $G_4(z)$ are the gradient strength and Δt is the duration. This sequence illustrates a single propagation where the occupation probability on the first qubit at site $n\Delta k$ moves to site $(n-1)\Delta k$, while the occupation number on the second spin advances to site $(n+1)\Delta k$. The shift of

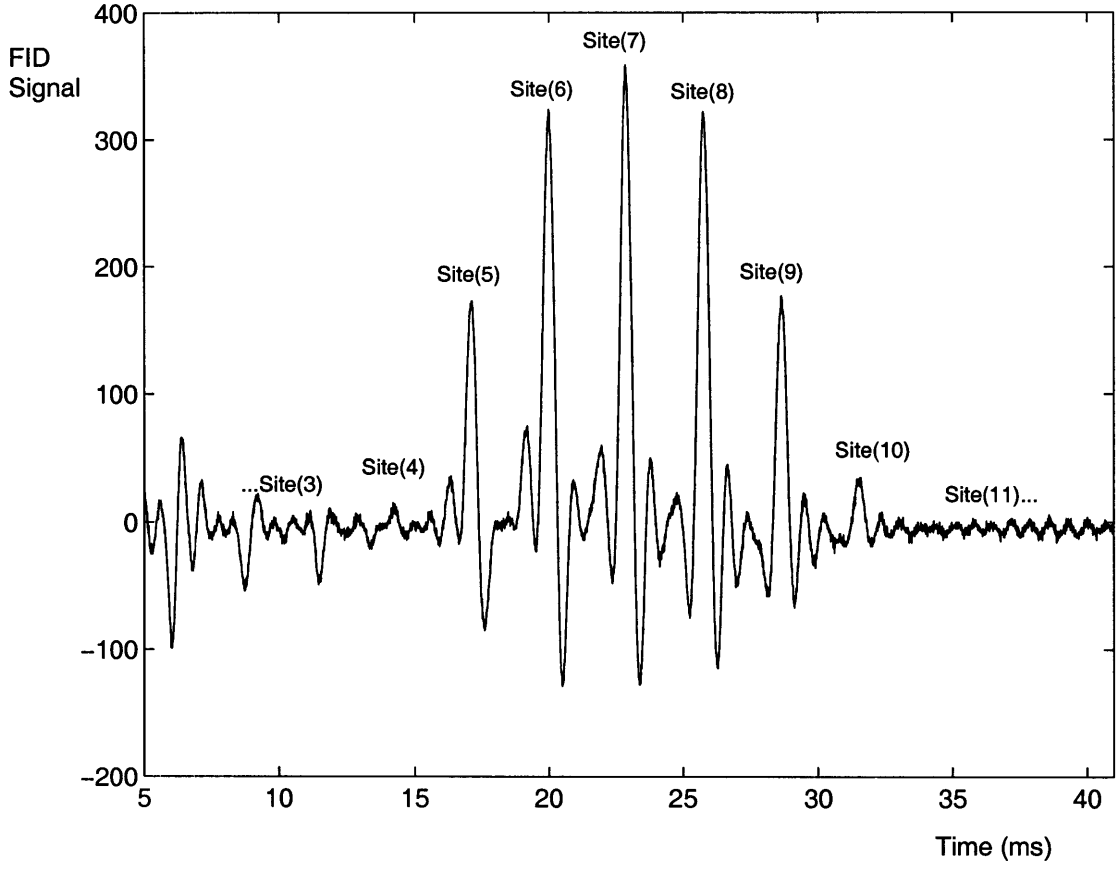

Figure 5-2: **Readout** Measurement on the hydrogen spin is illustrated here. The magnetization peaks are related to the occupation numbers at each lattice site by $n_i = \frac{1}{2}(1 + \sigma_z^i)$. The observed spectrum is imposed by a sinc function.

the k values should satisfy the following equation,

$$-\left(\Delta k_z^{1'} - \Delta k_z^1\right) = \Delta k_z^2 + \Delta k_z^{2'} = \Delta k. \tag{5.26}$$

Hence, the relation between two field gradients can be derived by

$$\frac{G_3(z)}{G_4(z)} = \frac{\gamma_H + \gamma_C}{\gamma_H - \gamma_C}. \tag{5.27}$$

Choose an identical time period Δt as in the lattice initialization step resulting in $G_3(z) = G_2(z)$ and $G_4(z) = G_1(z)$.

5.3 Conclusion and Discussion

The experimental mass densities are plotted in Fig. 5-3 with the exact analytical solutions. Four successive time steps of the quantum algorithm were implemented on 16 two-qubit sites.

Here, we demonstrate a single streaming step accomplished by the linear magnetic field gradient. Notice that contiguously applying the collision step and streaming step doesn't lead us to the numerical solution for the diffusion equation. However, it can be used to implement some type-I quantum lattice gas algorithms.

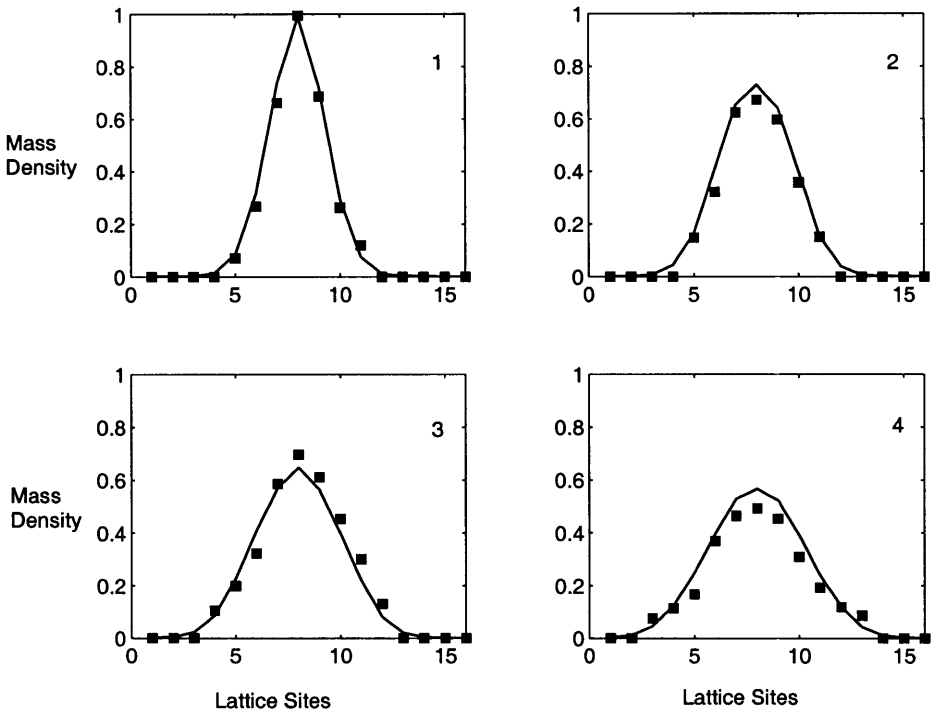

Figure 5-3: **k-space experimental data versus analytical solutions** The experimental data (dots) are plotted together with analytical solutions (solid lines) for four time steps on 16 two-qubit sites.

Chapter 6

Type-I Quantum Lattice Gas Algorithms

The difficulty of constructing, controlling and maintaining coherence in a single complicated quantum device makes an array of simple devices with fixed interations particularly attractive from the point of view of quantum computation. In this paradigm, a quantum computer is a quantum cellular automata (QCA): the state of each simple device in the array depends on the states of the cells in some local neighborhood at the previous time-step. QCA, therefore, provide a valuable test-bed for investigating both potential quantum computer architectures and algorithms. The study of QCA is probably originated with the interesting work of Grossing and Zeilinger [40, 41, 42]. However, their models are approximately quantum mechanical because they are not linear and unitary even though the probability is preserve. The first homogeneous quantum cellular automata was introduced by Meyer [8]. He also defined one particle quantum lattice gas algorithm which simulates one-dimensional Dirac equation. Boghosian and Taylor [43, 44, 45] and separately Succi [46, 47] have defined QLG models for the Schroedinger equation in D dimensions.

The QLG algorithms may be simulated on a quantum computer with realizable substantial speedup over classical hardware. Watrous [48] showed that any partitioned

[1]This section was extracted from an unpublished paper. This research is cooperated with Carlos Perez, University of Waterloo, Canada.

quantum cellular automata can be simulated by a quantum Turning machine. The first special quantum processor designed to directly realize quantum cellular automata is suggested by Seth Lloyd. Preliminary experimental designs have been proposed for ion traps, optical lattices and endohedral fullerenes on silicon [49, 50, 51].

Liquid state NMR has been proved to be an ideal way to explore many aspects of quantum computing and QIP. The success of NMR quantum computations means that large arrays of few entangled qubit quantum computers are already available now. We propose a QLG algorithm here and a potential design to implement the algorithm by nuclear magnetic resonance. A simple ring model has been chosen as the first test.

6.1 Quantum lattice gas algorithms

Usually, a random walk is simulated by selecting one particle in the system and transporting it at random upwards and downwards, provided that the destination site is empty. At each site z of the lattice, instead of only registrating the position of the particle, one also tracks down the directions by associating two binary values $n_1(z,t)$ and $n_2(z,t)$. These quantities present occupation numbers indicating whether or not a upward- or downward-moving particle is entering site z at time t, respectively. The random motion is obtained by shuffling the two directions of motion at each lattice site and at each time step. A upward-moving particle, entering site z at time $t+\Delta t$, must be the one with probability p moving in the same direction at the site $z-\Delta z$ at time t, and with probability $1-p$, it may be the one at the same site pointing downwards at site $z+\Delta z$ and time t. Therefore, the random walk rule can be expressed by a transition matrix,

$$A = \begin{pmatrix} p & 1-p \\ 1-p & p \end{pmatrix}. \tag{6.1}$$

The quantum lattice gas algorithms are the generalizations of classical lattice gas algorithms, introducing quantum mechanical features into the lattice. One may consider to replace a classical cell by a quantum state and the binary values associated

with each cell are denoted by complex values then [8]. The occupation numbers n_1 and n_2 map to the probability amplitudes $\psi_{z,\alpha}$ and $\psi_{z,\alpha'}$ of the position z, respectively. The single time step evolution is the composition of propagation and collision as described:

$$\begin{aligned} \sum \psi_{z,\alpha}|z,\alpha\rangle &\xrightarrow{propagation} \sum \psi_{z,\alpha}|z+\alpha,\alpha\rangle \\ &\xrightarrow{collision} \sum S_{\alpha,\alpha'}\psi_{z,\alpha}|z,\alpha'\rangle. \end{aligned} \tag{6.2}$$

where z is the current position of the particle and α indicates the directions. Then two

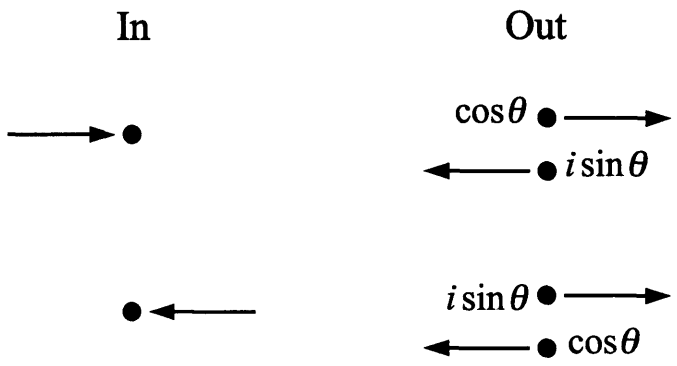

Figure 6-1: **Collision rules for 1D QLG algorithm** The collisions of the simplest one dimensional QLG algorithm. A single particle of mass $\tan\theta$ at a site has an amplitude to be scattered $i\sin\theta$.

directions of motions are shuffled in the collision step: the amplitudes and directions are changed by a uniform update rule $S_{\alpha,\alpha'}$ for all the sites. The collision operator

can be written as

$$S_{\alpha,\alpha'} = \begin{pmatrix} \cos\theta & i\sin\theta \\ i\sin\theta & \cos\theta \end{pmatrix}. \tag{6.3}$$

Then the particle propagates to the neighboring cell $|x+\alpha, \alpha\rangle$ associated with direction α or $|x-\alpha', \alpha'\rangle$ pointing to α' at time $t+\Delta t$. The evolution of the dynamic is given by repeating the actions of the update rules.

This algorithm described above requires a register of size $\log N$ where N is the number of lattice points. However, the above algorithm for a random walk of one particle does not generalize very nicely to k particles. It does not suffice to simply randomly shift the position of each particle, since if we are to admit any exclusion principle, then a particle cannot move to certain positions if those positions are already at maximum capacity. Say, if each position allows for only one particle, a particle can move there only if the site is empty. This requires one to check the current position of each other particles when updating the position of a particular particle. This approach requires $O(k \log N)$ bits of memory, and $O(k^2 \log N)$ for each update step. We will refer to this algorithm as a register approach, since it keeps the positions of each particle in different registers.

Here we propose a different generalization of classical lattice gas algorithm similar to the partitioned cellular automata mentioned by Morgolus [53], in which each lattice site is denoted by a single qubit. The dynamic of this system is easier to understand intuitively by taking the following picture. Two qubits are associated with one lattice site: qubits $\Psi(z,u,t)$ and $\Psi(z,d,t)$ represent the presence of a particle in the lattice point z at time t moving up or down, respectively. The update rule then consists of partitioning the lattice into a tiling set of contiguous pairs at each time step, such that the even and odd time step tilling overlap, depicted in Fig. 6-2. The values of each pair are then swapped with some probability amplitude. As long as the update operator u for each pair is unitary, so is the evolution of the whole lattice. The

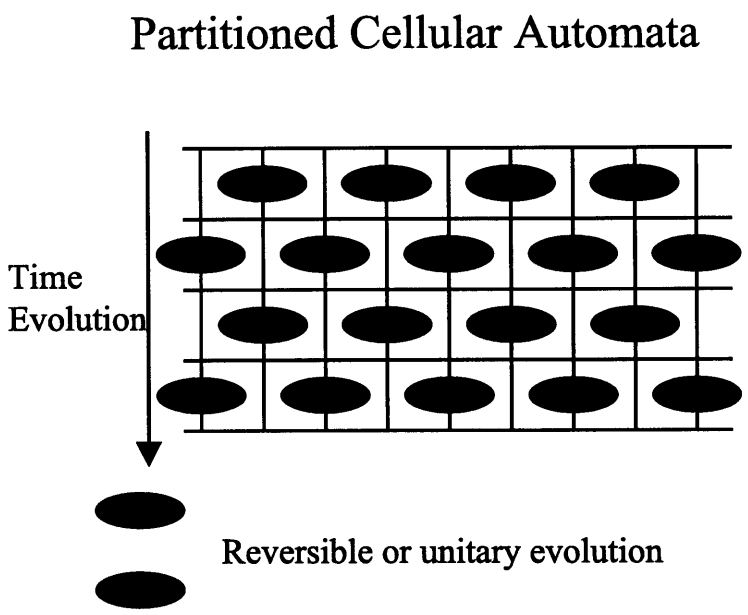

Figure 6-2: **Partitioned cellular automata** Each square represents a cell, and each oval is a unitary operator acting on two lattice cells. On odd/even steps the pairing is exchanged.

operator is defined as

$$u = \hat{C} = \begin{pmatrix} 1 & 0 & 0 & 0 \\ 0 & \frac{1+i}{2} & \frac{1-i}{2} & 0 \\ 0 & \frac{1-i}{2} & \frac{1+i}{2} & 0 \\ 0 & 0 & 0 & 1 \end{pmatrix}, \tag{6.4}$$

commonly called the *square-root-of-swap* gate. The system is evolved by repeated application of the unitary operators u. Suppose a system of an even number N of qubits, indicating N/2 lattice sites. Rewrite the gates in the odd and even time step as $U_{odd} = u^{\otimes N/2}$ and $U_{even} = 1 \otimes u^{\otimes N/2-2} \otimes 1$. Under the evolution $U = U_{even}U_{odd}$ we

have that:

$$\Psi(z,u,t+\Delta t) = \frac{1+i}{2}\Psi(z-\Delta z,d,t) + \frac{1-i}{2}\Psi(z+\Delta z,u,t)$$
$$\Psi(z,d,t+\Delta t) = \frac{1-i}{2}\Psi(z-\Delta z,d,t) + \frac{1+i}{2}\Psi(z+\Delta z,u,t). \tag{6.5}$$

Taking $\Psi(z,t) = \Psi(z,u,t) + \Psi(z,d,t)$ we can calculate the continuous limit using the Chapman-Enskog method [53]. We get that the evolution limits to

$$\frac{\partial}{\partial t}\Psi(z,t) = \frac{i}{2}\frac{\partial^2}{\partial z^2}\Psi(z,t), \tag{6.6}$$

which is exactly the Hamiltonian for a freely moving particle in one dimension.

In the automata defined above, we assume that all (randomized) swaps between contiguous cells are done in parallel in one time step. Hence, this approach requires $O(N)$ bits of memory and requires $O(1)$ time for each update step. This is particularly good if we take $k = \Omega(N)$, i.e. the number of particles is in the order of lattice points, which is generally expected in a lattice gas. This performance gain is, of course, assuming that a cellular automata is a realizable architecture, i.e. it is in fact possible to perform all the updates of a time step in parallel.

6.2 Chain Architectures

It has been suggested by Seth Lloyd [4, 5] that above algorithms can be implemented on a chain of repeated quantum spins. Consider a one dimensional chain of spin 1/2 systems, e.g. a polymer, with three different *species*, i.e $ABCABC\ldots$. The transition between the ground state and excited state of any quantum unit can be driven by applying a pulse at the resonant frequency. If A, B and C have distinct resonant frequencies, then they can be addressed independently. Consider only the nearest-neighbor interaction given by some (arbitrary) Hamiltonian H_{AB}, H_{BC}, H_{CA}. The effect of the interaction Hamiltonians is to shift the energy levels of each quantum unit corresponding to its neighbors. Hence, the resonant frequency ω_A takes distin-

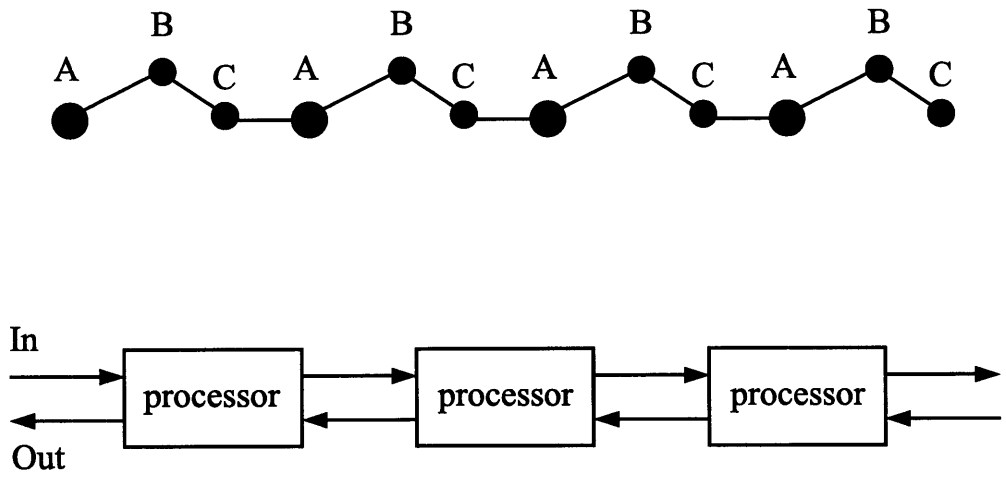

Figure 6-3: **Spin chain architectures** One-dimensional array of quantum units ($ABCABC\ldots$), such as nuclear spins in a polymer, is decipted here. A series of spins ABC can be treated as a quantum information processor. Sequence of resonant pulses allow one to load information and unload results at the end of an array. Each processor has the same circuit and they can process information and exchange it with the nearest neighbors.

guishable values ω_{00}^A, ω_{01}^A , ω_{10}^A , ω_{11}^A, depending on whether it's C and B neighbors are in the states 0 and 0, 0 and 1, 1 and 0, or 1 and 1. If these are all different, then transitions on species A spins can be done selectively depending on the value of its neighbors. For example, by applying a π pulse with frequency ω_{00}^A all species A lattice points whose both neighbors are in the state 0 will be flipped. It is also possible to apply any two qubit gates on all pairs A, B or C, A or B, C. Though originally proposed with three distinguishable qubit species, the model can easily work with more species [52]. These single qubit operations and two qubit gates can supply the logical operations and can be wired together to give any desired logic gate.

Input of information and readout of the results are through the end unit of the array which can be controlled independently because it has only one neighbor. One can load arbitrary information onto the end of the array and exchange the information with its neighbor. As a result, any sequence of desired information can be loaded onto A, B and C by continuing uploading at the end unit and swapping between different units.

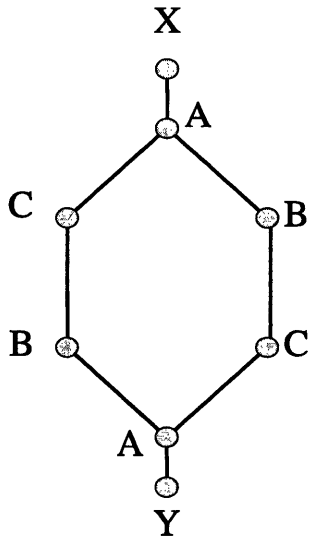

Figure 6-4: **The ring model** This model shows a chain of 6 quibts. Two loading qubits are presented by X and Y respectively. All the qubits with the same labels share the same resonant frequencies.

6.3 NMR Simulations

6.3.1 Spin System

A ring model, illustrated in Fig. 6-4, has been selected for the first study depending on the following four assumptions. (1) The ring is composed of two pairs of three distinguishable qubits ABC with qubits X and Y attached to A, served as loading

qubits. (2) Qubits A, B, C have the same Zeeman interaction with the applied magnetic field, but associated with different chemical shifts. The chemical shifts for qubit A, B and C are set to be $0Hz$, $4kHz$ and $8kHz$ respectively. (3) Only the nearest neighbor interactions have been taken into account and the scalar coupling constant is $50Hz$ altogether between ABC spins. The internal Hamiltonian of these spins, therefore, is

$$H_{internal} = -\frac{1}{2}\sum_{i=A}^{C}\omega_i\sigma_z^i + \frac{\pi J}{2}\left(\sigma_z^A\sigma_z^B + \sigma_z^B\sigma_z^C + \sigma_z^C\sigma_z^A\right) \tag{6.7}$$

where ω_i represent the chemical shifts of the spins and J are scalar coupling constants. (4) Loading qubits are several-hundred megahertz off-resonance and are not affected by any pulses applied to the ABC spins.

Unlike the labeled chloroform sample, the resonant frequencies are not widely separated, so that a RF pulse on resonance with one carbon spin will rotate all. Usually, a low-power RF pulse can be used to obtain selective operation on each qubit here. However, the selective pulses have disadvantage that low power implies long duration. This not only introduces errors due to relaxation, or decoherence, but also allows significant evolution under the action of the internal Hamiltonian. In the past, this evolution was rarely of concern because there was little importance placed on implementing a particular operation. Here, we use an alternative method with strongly modulating pulses to implement precisely the desired operations[31]. This allows us to use high-power pulses that strongly modulate the system's dynamics. These gates, shown in Table 6.3.1, allow arbitrary rotations of each spin, while refocusing the internal evolution.

6.3.2 Logic Gates

Information is initially stored in X and Y and a series of unitary transformations $\{U\}$ brings the information to other qubits. This set of unitary operators is essentially a series of two-qubit SWAP gates between adjacent qubits. A single two-qubit SWAP

Pulse	Time (μs)	Max. Power (kHz)	Discrete Fidelity
$\pi\|_x^A$	226.24	5.18	0.9989
$\pi\|_x^B$	267.35	4.87	0.9985
$\pi\|_x^C$	267.35	4.87	0.9985
$\frac{\pi}{2}\|_x^{AB}$	355.12	5.25	0.9983
$\pi\|_x^{AB}$	338.19	11.36	0.9973
$\pi\|_x^{BC}$	459	4.95	0.9977
$\pi\|_x^{AC}$	302.57	13.33	0.9985

Table 6.1: **Summary of the relevant characteristics for the set of transformations required for the implementation of QCA.** The three columns list the pulse duration (in μs), maximum power (in kHz), and the fidelity of simulated pulse.

gate for qubit A, B is

$$\begin{aligned} U_{swap}^{AB} &= \exp\left[i\frac{\pi}{4}(\sigma_x^A+\sigma_x^B)\right]\exp\left[-i\frac{\pi}{4}\sigma_z^A\sigma_z^B\right]\exp\left[-i\frac{\pi}{4}(\sigma_x^A+\sigma_x^B)\right] \\ &\quad \exp\left[-i\frac{\pi}{4}\sigma_z^A\sigma_z^B\right] \\ &\quad \exp\left[-i\frac{\pi}{4}(\sigma_y^A+\sigma_y^B)\right]\exp\left[-i\frac{\pi}{4}\sigma_z^A\sigma_z^B\right]\exp\left[i\frac{\pi}{4}(\sigma_y^A+\sigma_y^B)\right]. \end{aligned} \tag{6.8}$$

where the exponential terms proportional to $\sigma_z^A\sigma_z^B$ represent the internal Hamiltonian evolutions. Notice that the third spin C is also evolving under the internal Hamiltonian while applying a two-qubit operator. π pulses are applied to modulate the internal interaction terms, resulting in averaging the interaction with qubit C. The choice of this molecule is particular convenient because the scalar coupling constants are identical. Here, we demonstrate a scheme for implementing the operator in Fig. 6-5. Hence, the interaction term $\sigma_z^A\sigma_z^B$ can be recast as

$$\begin{aligned} \exp\left[-i\frac{\pi}{4}\sigma_z^A\sigma_z^B\right] &= \exp\left[-i\frac{\pi}{16}(\sigma_z^A\sigma_z^B+\sigma_z^A\sigma_z^C+\sigma_z^B\sigma_z^C)\right]\exp\left[-i\frac{\pi}{2}\sigma_z^C\right] \\ &\quad \exp\left[-i\frac{\pi}{16}(\sigma_z^A\sigma_z^B+\sigma_z^A\sigma_z^C+\sigma_z^B\sigma_z^C)\right]\exp\left[-i\frac{\pi}{2}(\sigma_x^A+\sigma_x^B)\right] \\ &\quad \exp\left[-i\frac{\pi}{16}(\sigma_z^A\sigma_z^B+\sigma_z^A\sigma_z^C+\sigma_z^B\sigma_z^C)\right]\exp\left[i\frac{\pi}{2}\sigma_z^C\right] \\ &\quad \exp\left[-i\frac{\pi}{16}(\sigma_z^A\sigma_z^B+\sigma_z^A\sigma_z^C+\sigma_z^B\sigma_z^C)\right]\exp\left[i\frac{\pi}{2}(\sigma_x^A+\sigma_x^B)\right]. \end{aligned} \tag{6.9}$$

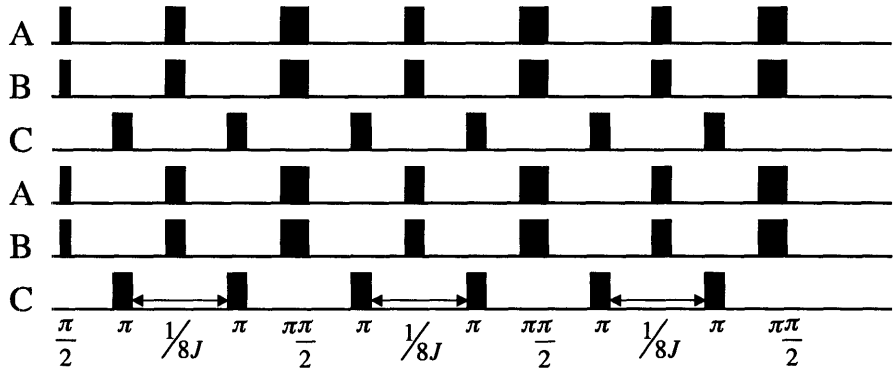

Figure 6-5: **The two-qubit SWAP gate** Here demonstrates the pulse sequence of the SWAP gate on two qubits and untouched the third spin. To refocus the scalar interactions between pair AC and BC, a π pulse has been performed on pair AB and separate the delay period to half. Two π pulses are performed on qubit C in the a quarter and three quarter of the delay respectively.

In summary, the usage of strong modulating pulses in conjunction with the selective evolution in 6.9 gives us the desired unitary operations to shift the information. The gate fidelities of these operators are listed in Table 6.3.2.

6.3.3 Methodology

One way to implement our QLG algorithm on a ABC chain is to map every 2 cells of the QCA lattice to three spins of the chains. For instance, only using A and B spins here results in a lattice of 4 cells. A single step of implementation of our QCA can be performed as following:

1. performing the update rule $\hat{C}_{AB}$ on pairs AB on odd iterations

2. exchanging the information on qubits BC

Gates	Gates Fidelity
U_{AB}^{swap}	0.9556
U_{BC}^{swap}	0.9443
$\hat{C}_{AB}$	0.9605
$\hat{C}_{CA}$	0.9582

Table 6.2: **Summary of the gates fidelities.** The two columns list the unitary operators, and the gate fidelity of them .

3. applying the same update rule on CA with $\hat{C}_{CA}$

4. then swapping BC again.

These operations are repeated until the mass density has evolved for the desired number of time steps.

Equation 6.4 shows the unitary operator used to update in each time step. These unitary matrix can be implemented by a similar manner described for the SWAP gates. Table 6.3.2 gives the simulated fidelities for $\hat{C}_{AB}$ and $\hat{C}_{CA}$.

Using the SWAP operators and the update unitary operators, we can translate QCA to experimental tasks as shown in Fig. 6-6. The lattice initialization step makes use of both the strong modulating pulses and the internal Hamiltonian to generate the desired unitary operation and shift the information. The repeated application of the update rules is accomplished by a similar way. The measurement is the reversed step of the lattice initialization.

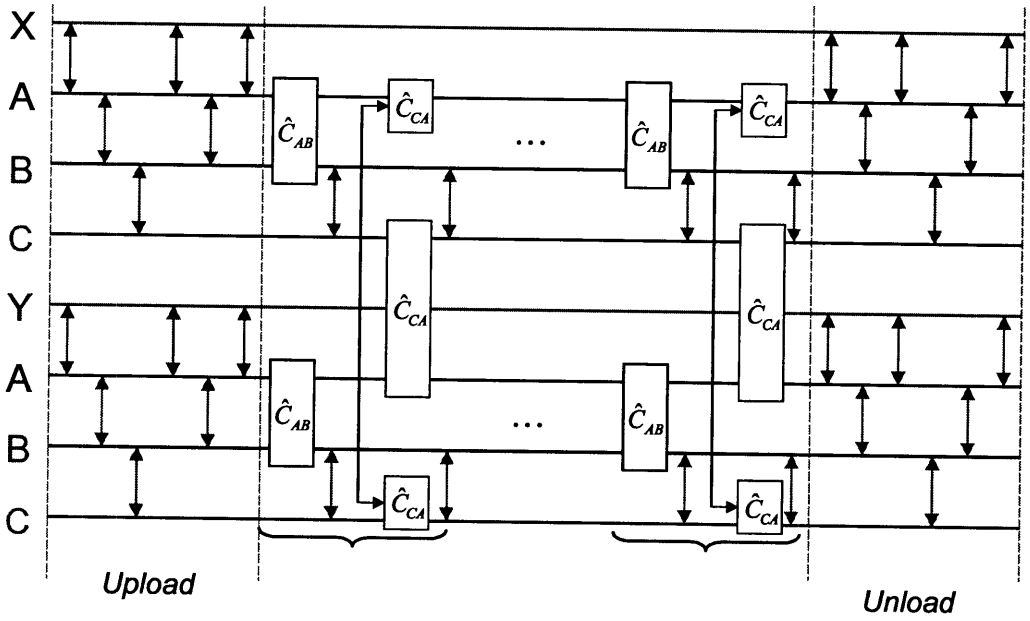

Figure 6-6: **One step QLG algorithm** The NMR implementation consists of three main section, each corresponding to the prescribed QCA step. The horizontal lines in the diagram correspond to RF pluses applied to each qubit respectively. In the encoding section, the initial magnetization is recorded on loading qubits before transferred to the other qubits. The unitary operator on pair AB and swap gate between BC follow the encoding. In the next step, the unitary operator on pair CA are applied, followed by swap gate between BC again.

Appendix A

Quantum Simulation using NMR

In 1982, Feynman recognized that a quantum system could efficiently be simulated by a computer based on the principle of quantum mechanics rather than classical mechanics [3]. This is perhaps one of the most important short term applications of QIP. An efficient quantum simulator will also enable new approaches to the study of multibody dynamics and provide a testbed for understanding decoherence. NMR has provided a valuable experimental testbed for quantum simulations. Here, We will briefly review some experiments other than the implementation of the quantum lattice gas algorithms.

A general scheme of simulating one system by another is expressed in Fig. A-1. The goal is to simulate the evolution of a quantum system S using a physical system P. The physical system is relatedto the simulated system via an invertible map ϕ, which creates the correspondence of states and the system S is mapped to $V = \phi U \phi^{-1}$. After the evolution of the physical system from state p to p_T, The inverse map brings it back to the final state $s(T)$ of the simulated system.

The first explicit experimental NMR realization of such a scheme was the simulation of a truncated quantum harmonic oscillator (QHO) [54]. The states of the truncated QHO were mapped onto a two-qubit system as follows

$$|n = 0\rangle \leftrightarrow |0\rangle|0\rangle \equiv |00\rangle$$

$$|n = 1\rangle \leftrightarrow |0\rangle|1\rangle \equiv |01\rangle$$

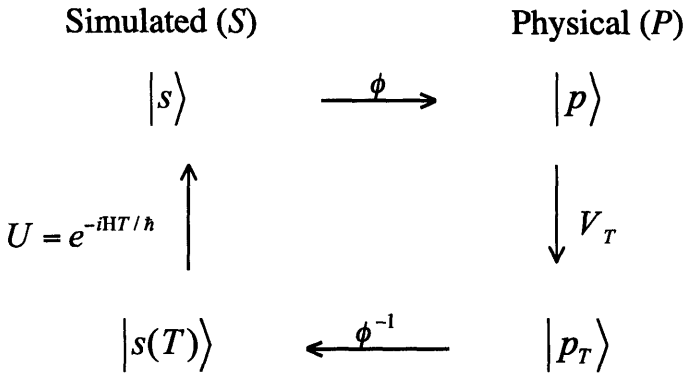

Figure A-1: **Quantum simulation scheme** Correspondence between the simulated and physical system. The initial state s evolves to $s(T)$ under the propagator U. This process is related to the evolution of state p in the physical system by an invertible map ϕ.

$$|n=2\rangle \leftrightarrow |1\rangle|0\rangle \equiv |10\rangle$$
$$|n=3\rangle \leftrightarrow |1\rangle|1\rangle \equiv |11\rangle \tag{A.1}$$

The propagator of the truncated QHO

$$U = \exp\left[-i(\frac{1}{2}|0\rangle\langle 0| + \frac{3}{2}|1\rangle\langle 1| + \frac{5}{2}|2\rangle\langle 2| + \frac{7}{2})|3\rangle\langle 3|\right] \tag{A.2}$$

(Ω is the oscillator frequency) was mapped onto the following propagator of a two-spin system

$$V_T = \exp\left[i(2I_z^2(1 - I_z^1) - 2)\Omega T\right]. \tag{A.3}$$

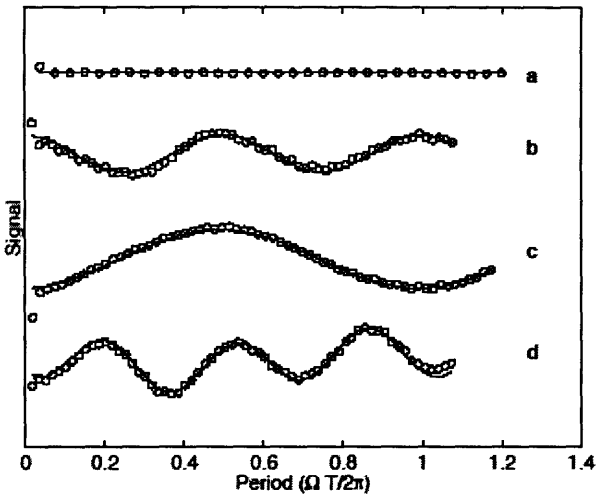

Figure A-2: **Truncated quantum harmonic oscillator** NMR signals demonstrate a quantum simulation of truncated harmonic oscillator. The solid lines are fits to theoretical expectations. Evolution of the different initial states are shown: (a) evolution of $|0\rangle$ with no oscillation (b) evolution of $|0\rangle + i|2\rangle$, showing 2Ω oscillations (c) evolution of $|0\rangle + |1\rangle + |2\rangle + |3\rangle$, showing Ω oscillation and (d) 3Ω oscillations.

Implementing this propagator on the 2−spin system simulates the truncated QHO as shown in Fig. A-2.

Quantum simulatin however is not restricted to unitary dynamics. It is sometimes possible to engineer the noise in a system to control the decoherence behavior and simulate non-unitary dynamics of the system [55]. Simple models of decoherence have been shown using a controlled quantum environment in order to gain further understanding about decoherence mechanisms.

In one model [56], the environment is taken to be a large number of spins coupled to a single system spin so that the total Hamiltonian can be expressed as

$$\mathcal{H} = \omega_1 I_z^1 + \sum_{k=2}^{N} \omega_k I_z^k + 2\pi \sum_{k=2}^{N} J_{1k} I_z^1 I_z^k \tag{A.4}$$

corresponding to the system, the environment, and the coupling between the system and the environment, respectively. The number of spins in a typical QIP NMR molecule is small, which makes the decoherence arising from the few system-environment

couplings rather ineffective, as the recurrence time due to a small environment is relatively short. This can be circumvented by using a second classical environment which interacts with a smaller quantum environment (see Fig. A-3 for an illustration of the model) [57].

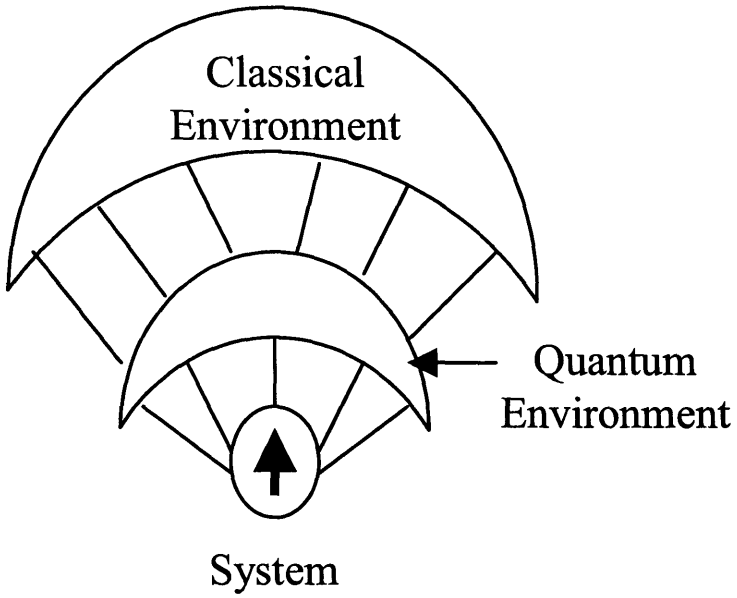

Figure A-3: **Demonstration of system and environment** Basic model for the system, local quantum and classical environment.

In this model, following the evolution of the system and the small quantum environment, a random phase kick was applied to the quantum environment. This has the effect of scrambling the system phase information stored in the environment during the coupling interaction and therefore emulates the loss of memory. When the kick angles are averaged over small angles, the decay induced by the kicks is exponential and the rate is linear in the number of the kicks. As the kick angles are completely randomized over the interval from 0 to 2π, a Zeno type effect is observed. Fig. A-4 shows the dependence of the decay rate on the kick frequency: the decay rate initially increases to reach a maximum and then decreases, thereby illustrating the motional narrowing or decoupling limit. This NMR-inspired nodel thus provides implementation of controlled decoherence yielding both non-exponential and exponential decays (with some control over the decay rates), and can be extended to investigate other

noise processes.

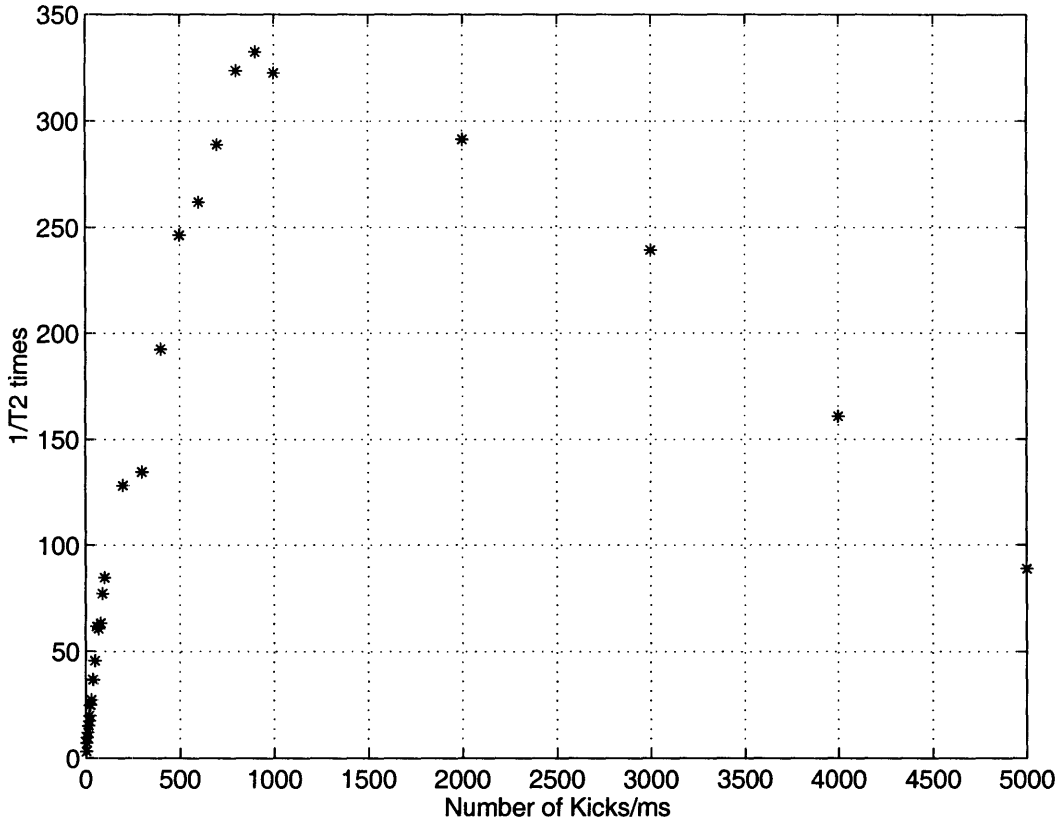

Figure A-4: **Decay rate** Simulation showing the dependence of the decay rate on the kick rate, and the onset of the decoupling limit. Beyond 900 $kicks/ms$ the decay rate decreases.

Bibliography

[1] M. A. Nielsen and I. L. Chuang. *Quantum Computation and Quantum Information.* Cambridge University Press, Cambridge, UK, 2000.

[2] P. W. Shor. Polynomial-time algorithms for prime factorization and discrete logarithms on a quantum computer. *Siam. J. Comput.*, 26:1484-1509, 1997.

[3] R. Feynman. Simulating physics with computers. *International Journal of Theoretical Physics*, 21(6-7):467-488, 1982.

[4] S. Lloyd. A potentially realizable quantum computer. *Science*, 261:1569-1571, 1993

[5] S. Lloyd. Universal quantum simulators. *Science*, 273:1073-1078, 1996.

[6] C. Zalka. Efficient simulation of quantum systems by quantum computers. *Progress of Physics*, 46:877-879, 1998.

[7] S. Wiesner. Simulations of many-body quantum systems by a quantum computer. quant-ph/9603028.

[8] D. A. Meyer. From quantum cellular automata to quantum lattice gases. *Journal of Statistical Physics*, 85:551-574, 1996.

[9] D. A. Meyer. On the absence of homogeneous scalar unitary cellular automata. *Physics Letter A*, 223:337-340, 1996.

[10] D. A. Meyer. Quantum mechanics of lattice gas automata: One-particle plane waves and potentials. *Physical Review E*, 55:5261-5269, 1997.

[11] J. Yepez. Type-ii quantum computers. *International Journal of Modern Physics C*, 12:1273-84, 2001.

[12] A. N. Emerton, P. V. Coveney, and B. M. Boghosian. Lattice-gas simulations of domain growth, saturation, and self-assembly in immiscible fluids and microemulsions. *Physical Review E*, 55:708-720, 1997.

[13] S. Chen, G. D. Doolen, K. Eggert, D. Grunau, and E. Y. Loh. Local lattice-gas model for immiscible fluids. *Physical Review A*, 43:7053-7056, 1991.

[14] C. Appert and S. Zaleski. Lattice gas with a liquid-gas transition. *Physical Review Letters*, 64:1-4, 1990.

[15] D.H. Rothman and S. Zaleski. Lattice-gas models of phase separation: interfaces, phase transitions, and multiphase flow. *Reviews of Modern Physics*, 66:1417-1479, 1994.

[16] B. Chopard, and M. Droz. Cellular automata. Cambridge University Press, Cambridge, UK, 1998.

[17] D. A. Wolf-Gladrow. Lattice-gas cellular automata and lattice boltzmann models. Springer-Verlag, Berlin, Heidelberg, 2000.

[18] J. Yepez. Quantum lattice-gas model for the diffusion equation. *International Journal of Modern Physics C*, 12:1285-1303, 2001.

[19] J. Yepez. Quantum lattice-gas model for burger's equation. *Journal of Statistical Physics*, 107:203-224, 2002.

[20] J. Yepez. Quantum lattice-gas algorithm for mhd. In preparation.

[21] R. R. Ernst, G. Bodenhausen, and A. Wokaun. *Principles of Nuclear Magnetic Resonance in One and Two Dimensions.* Oxford University Press, Oxford, 1994.

[22] D. G. Cory, A. F. Fahmy, and T. F. Havel. Ensemble quantum computing by nuclear magnetic resonance spectroscopy. *Procedings of the National Academy of Science*, 94:1634-1639, 1997.

[23] N. A. Gershenfeld and I. L. Chuang. Bulk spin-resonance quantum computation. *Science*, 275:350-356, 1997.

[24] M. Pravia, E. Fortunato, Y. Weinstein, M. D. Price, G. Teklemariam, R. J. Nelson, Y. Sharf, S. Somaroo, C. H. Tseng, T. F. Havel, and D. G. Cory. Observations of quantum dynamics by solution-state n. m. r. spectroscopy. *Concepts in Magnetic Resonance*, 11:225-238, 1999.

[25] A. N. Garroway, P.K. Grannell, and P. Mansfield. Image formation in n. m. r. by a selective irradiative process. *Journal of Physics C*, 7:457-462, 1974.

[26] T. F. Havel, Y. Sharf, L. Viola, and D. G. Cory. Hadamard products of product operators and the design of gradient-diffusion experiments for simulating decoherence by NMR spectroscopy. *Physics Letter A*, 280:282, 2001.

[27] E. Knill, R. Laflamme, R. Martinez, and C. H. Tseng. An algorithmic benchmark for quantum information processing. *Nature*, 404:368-370, 2000.

[28] L. M. K. Vandersypen, M. Steffen, G. Breyta, C. S. Yannoni, R. Cleve, and I. L. Chuang. Experimental realization of an order-finding algorithm with an NMR quantum computer. *Physical Review Letter*, 85:5452-5455, 2000.

[29] L. M. K. Vandersypen, M. Steffen, G. Breyta, C. S. Yannoni, M. H. Sherwood, and I. L. Chuang. Experimental realization of Shor's quantum factoring algorithm using nuclear magnetic resonance. *Nature*, 414:883-887, 2001.

[30] A. Sodickson and D.G. Cory. A generalized k-space formalism for treating the spatial aspects of a variety of n. m. r. experiments. *Progress in Nuclear Magnetic Resonance Spectroscopy.*, 33:77-108, 1998.

[31] E. M. Fortunato, M. A. Pravia, N. Boulant, G. Teklemariam, T. F. Havel, and D. G. Cory. Design of strongly modulating pulses to implement precise effective Hamiltonians for quantum information processing. *Journal of Chemical Physics*, 116:7599-7606, 2002

[32] P. J. Love, B. M. Boghosian and D. A. Meyer. Lattice-gas and lattice-Boltzman methods from the perspective of quantum computation. in praparation.

[33] M. D. Price, T. F. Havel, and D. G. Cory. Nuclear magnetic resonance spectroscopy: an experimentally accessible paradigm for quantum computing. *Physica D*, 120:82-101, 1998.

[34] J.A. Jones and E. Knill. Efficient refocussing of one spin and two spin interactions for n. m. r. quantum computing. *Journal of Magnetic Resonance*, 141:322-325, 1999.

[35] J.A. Jones. N. m. r. quantum computing. *Progress in Nuclear Magnetic Resonance Spectroscopy*, 38:325-360, 2001.

[36] H. K. Cummins, and J. Jones. Use of composite rotation to correct systematic errors in nmr quantum computation. *New Journal Physics* 2:1-2, 2000.

[37] J. Jones. arXive E-print quant-ph/0301019, 2003.

[38] M. A. Pravia, N. Boulant, J. Emerson, A. Farid, E. M. Fortunato, T. F. Havel, R. Martinez, D. G. Cory. Robust control of quantum information. *Journal of Chemical Physics*, 119:9993-10001, 2003.

[39] N. Boulant, J. Emerson, T. F. Havel, D. G. Cory and S. Furuta. Incoherent noise and quantum information processing. *Journal of Chemical Physics*, 121:2955-2961, 2004.

[40] G. Grossing, and A. Zeilinger. Quantum cellular automata. *Complex Systems*, 2:197-208, 1988.

[41] S. Fussy, G. Grossing, H. Schwabl, and A. Scrinzi. Nonlocal computation in quantum cellular automata *Physical Review A*, 48:3470-3477, 1993.

[42] G. Grossing, and A. Zeilinger. Structures in quantum cellular automata *Physica A*, 151:366-370, 1988.

[43] B. M. Boghosian, and W. Taylor. Quantum lattice-gas models for the many-body Schrodinger equation. *International Journal of Modern Physics C*, 8:705-716, 1997.

[44] B. M. Boghosian, and W. Taylor. Quantum lattice-gas model for the many-particle Schrodinger equation in d dimensions. *Physical Review E*, 57:54-66, 1998.

[45] B. M. Boghosian, and W. Taylor. Simulating quantum mechanics on a quantum computer. *Physica D*, 120:30-42, 1998.

[46] S. Succi. Numerical solution of the Schrodinger equation using discrete kinetic theory. *Physical Review E*, 53:1969-1965, 1996.

[47] S. Succi, and R. Benzi. Lattice Boltzmann equation fro quantum mechanics. *Physica D*, 69:327-332, 1993.

[48] J. Watrous. *Proceedings of the 36th annual meeting on the funndations of computer science*, 528-537, 1995.

[49] B. C. Travaglione, and G. J. Milburn. Implementing the quantum random walk. *Physical Review A*, 65:032310, 2002.

[50] W. Dur, R. Raussendorf, V. M. Kendon, and H. J. Briegel. Quantum walks in optical lattices. *Physical Review A*, 66:052319, 2002.

[51] J. Twamley. Quantum-cellular-automata quantum computing with endohedral fullerenes. *Physical Review A*, 67:052318, 2003.

[52] S. C. Benjamin, and N. F. Johnson Cellular structures for computation in the quantum regime. *Physical Review A*, 60:4334-4337, 1999.

[53] T. Toffoli, and N. H. Margolus. *Cellular Automata Machines.* The MIT Press, Cambridge, Massachusetts, 1987.

[54] S. Somaroo, C.-H. Tseng, T.F. Havel, R. Laflamme, and D.G. Cory. Quantum simulations on a quantum computer. *Physical Review Letters*, 82:5381-5384, 1999.

[55] D. Bacon, A. M. Childs, I. L. Chuang, J. Kempe, D. W. Leung, and X. L. Zhou. Universal simulation of Markovian quantum dynamics. *Physical Review A*, 64:062302, 2001.

[56] W. H. Zurek. Environment-induced superselection rules. *Physical Review D*, 26:1862, 1982.

[57] G. Teklemariam, E. M. Fortumato, C. C. Lopez, J. Emerson, J. P. Paz, T. F. Havel, and D. G. Cory. Method for modeling decoherence on a quantum-information processor. *Physical Review A*, 67:062312, 2003.